

LUND UNIVERSITY  
MEDVISO

SIMULATING METAL CT ARTEFACTS FOR GROUND  
TRUTH GENERATION IN DEEP LEARNING.

MASTER'S THESIS IN BIOMEDICAL ENGINEERING

AUTHOR:  
Arthur Barakat

SUPERVISOR:  
Einar Heiberg

CO-SUPERVISOR:  
Karolina Gottschalk



DEPARTMENT OF BIOMEDICAL ENGINEERING

YEAR 2023



# Abstract

CT scanning stands as one of the most employed imaging techniques used in clinical field. In the presence of metal implants in the field of view (FOV), distortions and noise appear on the 3D image leading to inaccurate bone segmentation, often required for surgery planning or implant design. In this research project, we focused on developing a pipeline to create a rich ground truth dataset, forming the foundation for training a deep-learning bone segmentation algorithm capable of great results even in the presence of metal artefacts.

In order to build an extensive artefact-contaminated database, metal-free datasets were collected and bone delineated using Segment 3DPrint automatic bone-segmentation tool. Realistic metal implants were then designed in proper anatomical locations and synthetic artefacts generated using a MATLAB-based algorithm. The effectiveness of the simulator has been tested on real data using an anthropomorphic hand phantom with metal implants inserted and scanned with standard clinical CT parameters.

The simulator has proven to successfully mimic physical phenomena such as beam hardening, phantom starvation and noise which are the underlying causes of real metal artefacts. It produces realistic artefacts shapes, even for complex metal configurations. Additional datasets already exhibiting metal artefacts were also added to the database. The simulator was used there only to virtually rescanned those datasets for augmentation reasons.

Finally, a training pipeline was imagined using the artefact simulator in parallel to the training process. Data can thus be constantly augmented with new features as the training of the network is running.



# Abbreviations

<b>2D</b>	2 Dimensional
<b>3D</b>	3 Dimensional
<b>BHC</b>	Beam Hardening Correction
<b>CNN</b>	Convolutional Neural Networks
<b>CT</b>	Computed Tomography
<b>DL</b>	Deep learning
<b>FBP</b>	Filtered Back Projection
<b>FOV</b>	Field of View
<b>FP</b>	Forward Projection
<b>HU</b>	Hounsfield value
<b>LI</b>	Linear Interpolation
<b>MAR</b>	Metal Artefact Reduction
<b>MRI</b>	Magnetic Resonance Imaging
<b>SS</b>	Stainless Steel
<b>SUS</b>	Skåne University Hospital



# Acknowledgements

I would like to express my gratitude to who have made this thesis journey an enjoyable one, filled with great ideas, humor and invaluable guidance.

First and foremost, I would like to acknowledge Prof. Einar Heiberg for giving me the opportunity to embark on this project. His belief in my ability and ideas have been valuable for shaping the outcome of this thesis.

This thesis would have been "definit-Lee" less entertaining without my dear Bosnian friend and colleague, Muris, who introduced me too Loren, cepavici and given me this irresistible urge to 3D print everything.

I extend my heartfelt appreciation to the entire Medviso team who not only embraced my unique "Swenglish" but gave me great advice and support all along this thesis. Despite the early Friday morning meetings, it has been a pleasure working and learning with you.

I extend my sincere thanks to everyone who helped me along the way and provided me with great conversation and valuable help. I am especially thankful to PHD student and physicist Veronica Fransson for her invaluable assistance throughout the experimentation phase. Her time and advice have been truly beneficial for the outcome of this thesis.

I am particularly grateful to the Cardiac MR research group for welcoming me into their world and showing me that even the most brilliant minds can face technological challenges and wrestle with misbehaving microphones.

Finally, I would like to express my deep gratitude to Prof. Hanna Isaksson for introducing me to the research field in a first place and directing me towards this captivating thesis project.





# Contents

<b>Abstract</b>	<b>i</b>
<b>Abbreviations</b>	<b>iii</b>
<b>Acknowledgements</b>	<b>v</b>
<b>1 Introduction</b>	<b>9</b>
1.1 Context and motivation . . . . .	9
1.2 Purpose . . . . .	10
1.3 Previous work . . . . .	10
1.4 Delimitation . . . . .	11
<b>2 Background</b>	<b>13</b>
2.1 Physic behind CT imaging . . . . .	13
2.2 Metal artefacts . . . . .	14
2.3 MAR methods . . . . .	16
2.3.1 Hardware-based MAR methods . . . . .	16
2.3.2 MAR algorithms . . . . .	17
<b>3 Methods</b>	<b>19</b>
3.1 Pipeline . . . . .	19
3.2 Benefits of the implemented pipeline . . . . .	19
3.3 Data collection . . . . .	20
3.4 Generation of a metal artefact database . . . . .	21
3.4.1 Design and placement of the synthetic metal implants . . . . .	21
3.4.2 Materials used for the synthetic implants . . . . .	24
3.4.3 Simulation of metal artefacts . . . . .	25
3.4.4 Fanbeam and radon projections . . . . .	30
3.5 Architecture and training of the U-Net . . . . .	33
3.5.1 Architecture of the network . . . . .	33
3.5.2 Generation of label classes . . . . .	34
3.5.3 Data augmentation . . . . .	35

3.6	Training . . . . .	36
3.7	Metal artefacts assessment . . . . .	37
<b>4</b>	<b>Results</b>	<b>43</b>
4.1	Visual assessment of simulated artefacts . . . . .	43
4.2	Quantitative evaluation of simulated artefacts . . . . .	43
<b>5</b>	<b>Discussion</b>	<b>49</b>
5.1	Limitations . . . . .	49
5.2	Future work . . . . .	50
<b>6</b>	<b>Conclusion</b>	<b>53</b>
<b>7</b>	<b>Appendix</b>	<b>55</b>
	<b>References</b>	<b>lxi</b>

# 1. Introduction

## 1.1 Context and motivation

Computed tomography (CT) is a 3-dimensional (3D) imaging technique based on attenuation measurements of X-rays. It is nowadays clinically used to differentiate tissue types and contribute both to diagnosis and treatment planning. However, in the presence of strongly attenuating objects in the field of view (FOV), major artefacts are created in the reconstructed images [1]. In medical CT, these artefacts are often caused by metal parts implanted in the patient's body which degrade the image quality. As a consequence, the visualisation of certain structures or tissues can become difficult or even impossible. Metal artefacts are generally streak shaped and result from a combination of three main physical phenomena: beam hardening, scatter and noise [2]. For metal objects close to the tissues of interest, Hounsfield values from the CT reconstruction can be overly contaminated leading to dark zones interpreted as air or very bright areas mistakenly seen as metal or bone. This presents a major issue for the segmentation of specific tissues.

In the medical field, segmentation is defined as the process of identifying pixels on a medical image (such as CT, Magnetic Resonance Imaging (MRI)) that belong to the same object or structure of interest such as organs or tumors. Segmentation is a prerequisite for all image quantification. Segmentation has seen a huge progress with the use of deep-learning (DL) introduced in the early 2010s and later used in medicine [3]. DL enabled robust semi or fully automatic segmentation processes that, for some applications, have replaced fully manual delineations which are often time-consuming and practitioner-dependant. DL-based segmentation has now been widely used in clinical routine to facilitate and improve diagnosis and treatment planning but still suffers from poor results when confronted with metal artefacts. For instance, software such as Segment 3DPrint offer the possibility for automatic bone segmentation from CT images and is today clinically used. Segmented bones can then be used to design cutting guides, implants or plan surgery. However, the DL-based segmentation tool in Segment 3DPrint was not trained to properly segment bones when metal artefacts were included in the image volume. Improv-

ing the segmentation tool to overcome artefacts would save time for clinical practitioner and was thus the main aim of this thesis.

## 1.2 Purpose

Many semi or fully automatic segmentation tools, robust to metal artefacts, are already implemented in the research area [4]. However, to the best of the author's knowledge, no similar tool is already widely used in clinical routine. Consequently, the final purpose of this thesis is to take techniques to make algorithms less sensitive to metal artefacts into clinical routine. An already DL-based segmentation tool developed by Medviso and in used in multiple hospitals was thus improved to handle metal artefacts.

In this perspective, clinical CT scans were collected and multiple synthetic metal implants were designed for each dataset and used for the generation of complex and realistic synthetic artefacts. This augmented database was created in the prospect to use it in the future as a ground truth to train a DL bone segmentation tool that would be robust to metal artefacts and employed for clinical application.

## 1.3 Previous work

Medviso is a Sweden-based company providing image analysis software worldwide for both research and clinical applications. In the software Segment 3DPrint, multiple DL-based segmentation algorithms are implemented to extract various structures from images of the patients (bones, vessels, trachea, lungs, mandible, orbits, fetus and hearts for children with congenital heart disease) from both CT and MRI images. This thesis primarily focused on the automatic DL-based bone segmentation for CT images.

The current DL bone-segmentation process uses a 2D-U-net network structure based on the work of Ronneberger et al in 2015 [5]. U-Net network architecture is a one of the most implemented DL networks for medical image segmentation [3]. In the absence of metal in the CT scan, the U-Net network obtained good bone-segmentation results (Dice score:  $0.96 \pm 0.02$ , Jaccard score:  $0.93 \pm 0.04$ ). However, it was not trained to handle metal artefacts. Whenever confronted to artefacts, due to the presence of metal parts in the patient's body, regions were mistakenly labelled. Indeed, volumes where Hounsfield values were higher than normal due to artefacts were labelled as bone. On the

contrary, regions that were darkened by artefacts were labelled as background. Such results resulted in time consuming delineations for clinicians.

## 1.4 Delimitation

The delimitation of this project includes the use of the same architecture and hyperparameters for the 2D U-Net network. U-Net architecture has proven successful for segmentation in a vast number of biomedical applications and is both fast and accurate compared to other networks [3]. Investigating other networks was thus not in the scope of this thesis.

The network used is a 2D U-net and was originally trained with 20 datasets and tested with 21 datasets. They were carefully partitioned in order to keep scans of regions spread in the whole body for both partitions. The age, gender and scanner used were as diverse as possible, especially for the test datasets to comply with the U.S. Food and Drug Administration (FDA) requirements. A similar approach was used to build the ground truth database for the artefact-robust segmentation tool. However, the number of datasets was doubled to offer more variety. Further description of the CNN is available in the section [3.5](#)



## 2. Background

### 2.1 Physic behind CT imaging

CT imaging is based on the measurements of polychromatic X-rays intensities being attenuated when traveling through matter. Let's first consider a monoenergetic X-ray passing through an homogeneous object of linear attenuation  $\mu$ . Along this path  $L$ , the final intensity  $I$  of the beam, under ideal conditions (no beam hardening, noise or scatter), is described by Beer's law (2.1):

$$I = I_0 e^{-\mu x} \quad (2.1)$$

with  $I_0$  being the initial intensity of the X-ray and  $x$  the distance travelled by the ray along the path  $L$ .

For a heterogeneous object, the initial Beer's law (2.1) becomes:

$$I = I_0 e^{-\int_L \mu(x_j) dl} \quad (2.2)$$

With  $j$  denoting each compound.

For a polychromatic beam, similarly to clinical CT beams, both the intensity of the X-ray and the attenuation coefficients energy-dependency had to be considered. The previous equation (2.2) becomes:

$$I = \int I_0(E) e^{-\int_L \mu(x_j, E) dl} dE \quad (2.3)$$

Moreover, one assumed that the number of photons reaching the detector follows a Poisson distribution that can eventually be contaminated by extra scattered photons [6]. The intensity measurements can thus be modelled as follows:

$$Y \sim \text{Poisson} \{I + r\} \quad (2.4)$$

with  $r$  accounting for the mean number of background events and read-out noise variance [7] and assumed to be a non-negative constant [8] [9].

In order to get the projection values, the previous equations [2.4](#) and [2.3](#) can be expressed as follows :

$$P = -\ln\left(\frac{Y}{\int I_0(E)dE}\right) \quad (2.5)$$

This last equation [2.5](#) models the physic shaping attenuation coefficient measurement for polychromatic X-rays.

In conventional CT, attenuated X-rays intensity is measured along multiple lines  $L_i$  within a plan in order to later reconstruct an image. The measurement geometry for CT is fan-beam based with the X-ray tube rotating around the patient's body (see Figure [2.1](#)). The projection profiles are then stacked and stored as a sinograms where angular and radial samplings are used for axis (see Figure [2.1](#)). This process is called forward projection and constitute the first step in CT image acquisition.

The data is then filtered. Without filtering, the reconstructed images would display a significant blurring. This blurring is called '1/r blurring' as it decreases with the distance  $r$  from the center of the FOV. It can be removed with sharpening (high pass) filters.

Finally, the image is reconstructed using back projection. The full process is called filtered back projection (FBP) and is clinically the most widely used reconstruction technique as it is a fast, and straightforward [\[10\]](#). The measurements of the attenuated rays enables the reconstruction of an attenuation coefficient map representing the tissues radiated by the X-rays. It is by convention expressed relatively to water and air linear attenuation coefficients as follows [2.6](#):

$$HU = 1000 \frac{\mu - \mu_{\text{water}}}{\mu_{\text{water}} - \mu_{\text{air}}} \quad (2.6)$$

Both FP and FBP processes used for CT image acquisition are described in the figure [2.1](#)

## 2.2 Metal artefacts

Metal objects exhibit great attenuating properties compare to human tissues, especially soft ones. Therefore, they can generate artefacts due to beam hard-



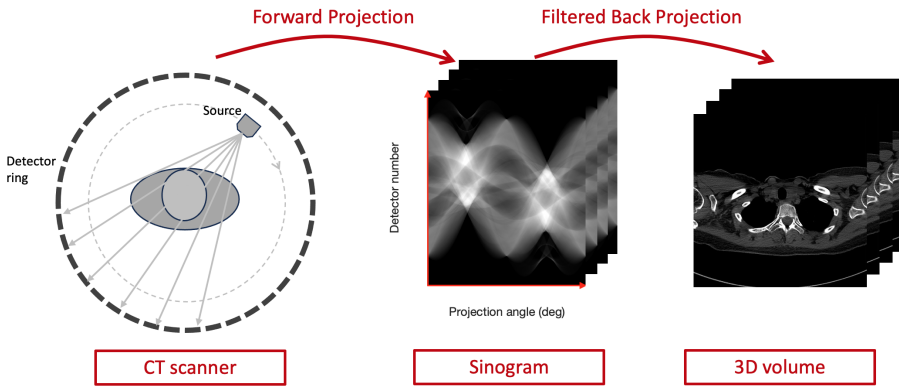


**Figure 2.1:** Overview of a standard CT scanning process from image acquisition to FBP

ening, scattering and photon starvation phenomena [11].

**Beam hardening:** Beam hardening occurs when using polychromatic X-ray beams which is the case for medical CT. Photons with the lowest energies are more attenuated than high energy photons, especially when dense objects are in the FOV. Attenuation of low energy photons is mostly caused because of photoelectric effect.

Photoelectric effect is particularly strong with materials of high atomic number  $Z$ , such as metals, and low energy photons. Indeed, the probability of this phenomenon to occur is proportional to  $\frac{Z^3}{E^3}$  with  $E$  being the energy of the photons [12]. The phenomenon is similar to a high pass filter and results in the mean beam energy to increase. The beam is thus 'hardened'. Locally, it will be interpreted as if photons travelled through a low-attenuating object which produces dark streaks in the reconstructed image. Dark streaks are mostly appearing along the axis of greatest attenuation. It is thus where the object is the longest in the 2D slice or between two metal objects (see Figure 2.2).

**Compton scattering:** At high energy, Compton scattering is dominant in CT as it is only proportional  $\frac{1}{E}$ , and not  $\frac{1}{E^3}$ . Photons are deviated from their initial trajectory inside the patient's body. Scattered photons then hit detectors that are not aligned with the central axis of the incident beam. This leads to false reconstruction and when combined with strong photoelectric effect, it leads to dark streaks on the reconstructed image as both phenomena lead to more photons being detected.

**Phantom starvation and noise:** If a significant part of the photons are ab-

sorbed because of highly-attenuating objects in the FOV, an insufficient number of them then reach the detectors leading to higher statistical errors of the projection data. This phenomenon known as phantom starvation is responsible for thin dark and bright streaks in the reconstructed image [13] [14].

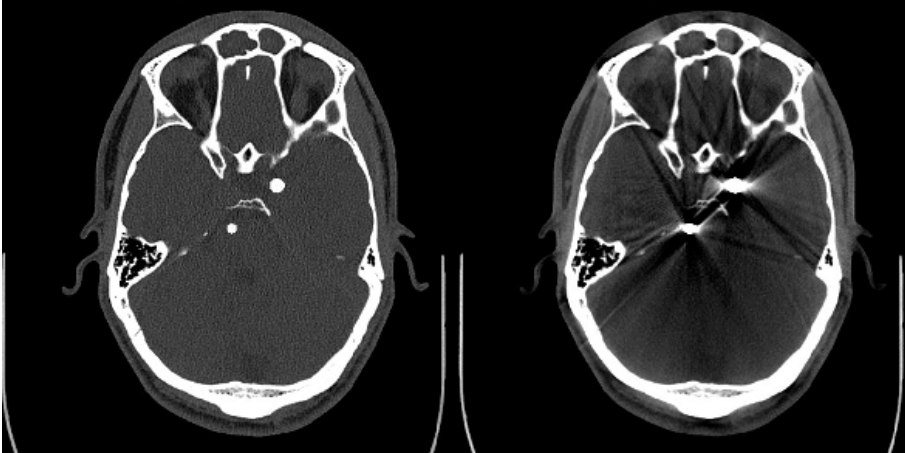


**Figure 2.2:** Metal artefacts simulated (Right) from the initial scan (left) with two virtually added ball-shaped coils.

However, multiple methods were developed to reduce metal artefacts and are known as MAR methods.

## 2.3 MAR methods

### 2.3.1 Hardware-based MAR methods

It is possible to reduce artefacts by changing the scan parameters or hardware used.

In radiography, the beam can be 'prehardened' by placing a metal sheet between the source and the patient which filters low energies. Metal artefacts can also be reduced by increasing tube voltage. It allows better penetration of high density objects leading to less photon starvation. However, it increases the dose received by the patients which can lead to health issues if too high. Dual energy scanning is also used to reduce metal artefacts. Two different tube voltages are used to perform the measurements and linear attenuation coefficients are then compared to reconstruct an image with less artefacts and more contrast (see Figure 2.3).

Nowadays, many scanners are also equipped with built-in MAR algorithms.

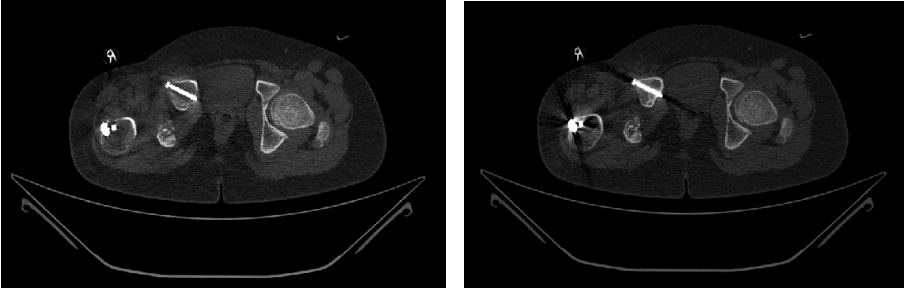


**Figure 2.3:** Example image when using dual energy (left) and without (right).

### 2.3.2 MAR algorithms

MAR algorithms are considered as post-processing techniques and can be classified into three distinct groups: physical effects correction, interpolation in projection domain and iterative reconstruction [15]. Physical effect corrections are often based on simple models which correct beam hardening [16] [17] and photon starvation [18]. However, it can fail to reduce strong artefacts caused by highly attenuating material such as metal. Interpolation methods are used to remove metal-affected data and replace the missing information with interpolation techniques. Linear interpolation (LI) is a common MAR method but can introduce new artefacts around the metal part. Iterative reconstruction methods are also used but are very computationally demanding.



# 3. Methods

## 3.1 Pipeline

The general pipeline of this thesis is described in the flowchart below (3.1). First, 75 CT images were collected and bones delineated. Metal implants were then designed with realistic clinical shapes and inserted as binary objects into the metal-free CT volumes similarly to real implants. Synthetic artefacts were then generated using an in-house developed software written in MATLAB [19] and inspired from [4]. Then for both metal-free and scans with metal, an artefact mask was created. Datasets were split into training data and test data (see Tables 7.1 and 7.2) according to a logic described in Section 3.5.

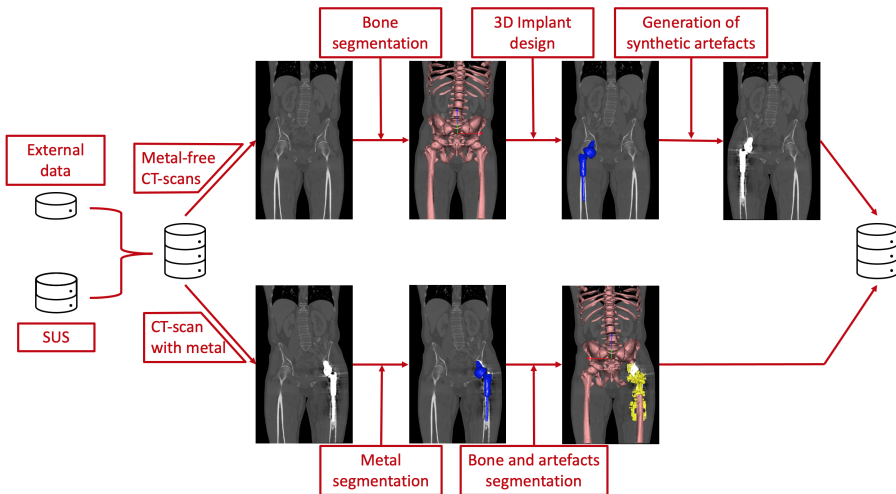


Figure 3.1: Thesis pipeline

## 3.2 Benefits of the implemented pipeline

The previously described pipeline (3.1) is essentially built around the simulation of synthetic artefacts. Indeed, training and testing data were mostly generated

by simulating metal artefacts as only a small number of datasets already contained metal and artefacts. It could have been possible to use solely images with real metal artefacts but it was less efficient for the following reasons:

- The use of the already implemented DL bone-segmentation tool saved time when the delineating bones. With real metal artefacts, many hours per image volume were required to obtain a good delineation as significant manual processing was needed.

- In addition, for datasets exhibiting strong artefacts, manual, delineation could be very laborious and uncertain, especially for dense artefacts between two close metal parts. For instance, in the case of a bilateral total hip replacement, the region between the prosthesis is entirely erased by the artefacts in the reconstructed image.

- Finally, for the U-Net network to be well trained and suited to handle various bone segmentation with different artefacts and implants, it was important to gather in the input data a great amount of medical images with artefacts of countless types. Collecting medical images with very different scanning parameters and implants in term of size, shapes, material and placement is challenging. Generating synthetic artefacts offers unlimited possibilities and artefacts shapes for a single scan providing us with great possibility for data augmentation.

### 3.3 Data collection

A total of 75 anonymised CT volumes were used in this project to create a rich database that would ensure robustness for the future bone-segmentation algorithm. Data was gathered from cases referred to creation of anatomical models at 3D Centre at Skåne University Hospital (SUS) as well as data downloaded from publicly available image repositories. CT images were collected from scanners manufactured by all four main CT scanner vendors (Phillips, GE, Siemens and Toshiba) resulting in an algorithm that should not be vendor-specific. The scans were also performed with different scanning parameters and reconstruction algorithm and a particular focus was put on selecting scans from different anatomical regions of the body in order to cover most parts of the body. Moreover, the age, gender and potential fractures and pathologies of the patients were also considered when selecting the datasets. Age and gender can affect significantly bone composition as they are for instance both considered as major non-modifiable factors risks in the development of osteoporosis.

Osteoporosis being a bone disorder that induces a decrease in bone mass and a significant deterioration of bone micro-structure which affects how bones are seen on a CT scan. Patient’s family background, ethnicity, physical activity or eating habits were not considered even if it could affect bone density with potential remodelling or bone disorders. Finally, scans were also selected taking into account acquisition dates. As the scanning technology greatly evolved the last three decades, a wide representation image acquisition technologies was ensured with the oldest scan obtained in 1990 and the latest in 2022. All scans details can be found in Tables [7.2](#) and [7.1](#) in appendix.

Among the 75 datasets, 19 contained real metal implants. These metal datasets were mainly used for two reasons. In the training, process, it is valuable to have real artefacts in case the simulation of synthetic artefacts would be slightly biased despite all precautions. For the validation, it is important to test the automatic DL bone-segmentation on real cases with non-synthetic artefacts. In the end, the segmentation will be performed on real clinical cases with real metal artefacts, not synthetic ones.

Synthetic implants were then designed and inserted within each metal-free datasets to later generate synthetic artefacts.

## 3.4 Generation of a metal artefact database

### 3.4.1 Design and placement of the synthetic metal implants

Metal implants are found to be customised and placed in very divers anatomical positions on the patient. They can exhibit very distinct sizes, shapes and materials [\[20\]](#). As a consequence, the metal implants inserted in the metal-free datasets were designed to capture this diversity and ensure a robust training for the DL network.

A substantial part of the implants were designed directly with the software Segment 3DPrint version 4.0 R11487 [Medviso, [segment.heiberg.se](http://segment.heiberg.se)] as it offers easy and powerful tools to generate customised plates, cranial implants, screws and rods. More complex implants such as hip prosthesis or pacemakers were designed using the industrial CAD software Fusion 360 [Autodesk Fusion 360 © 2020 Autodesk, Inc, version 2.0.16007 x86\_64]. This later software enables more freedom in the design process. The positioning of the implants designed with fusion 360 was performed directly on the software. The bones segmented with Segment 3DPrint were imported, as an STL file, to fusion 360. The implant was then properly placed in the right anatomical location relatively to the imported bones. The implant and its coordinates were

then saved and exported as an STL object. It was then opened with Segment 3DPrint and stored with the other synthetic implants designed locally. For each case, up to ten different customised implants were designed. The implants created are described below relatively to their anatomical position:

**Cranial region:** The main implants found in the upper part of the skeletal system are coiling, cranial and maxillofacial implants and dental filling. Coiling consist of thin metal threads inserted through the arteries to fill aneurysm. The final shape resembles a sphere of diameters ranging from a few millimeters for small aneurysm to more than 30 mm for the most severe cases [21]. Coiling was thus modelled using ball-shaped designs of corresponding sizes that were placed in the brain region (see Figure 3.2). A pattern could be added to the ball to slightly alter the shape and the filling. For Cranial defects, it is usually a significant part of the skull that is damaged or missing. Mesh or filled implants are clinically used to cover cranial defects and protect the brain. Dental filling and brackets were also inserted on the teeth when possible. Plates, screws and rods were also designed.

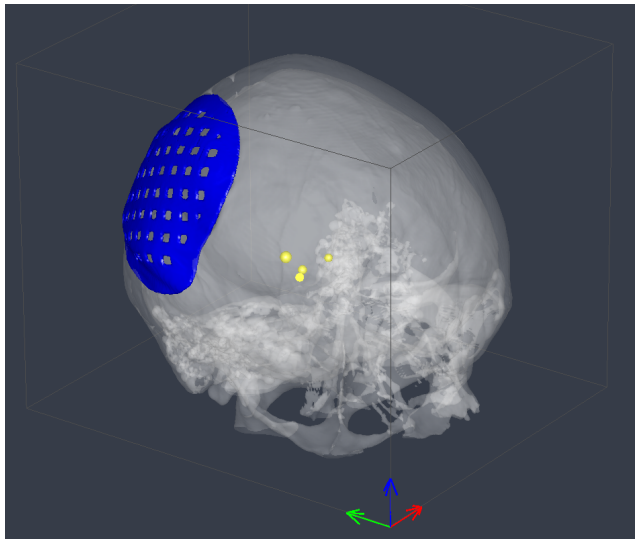


**Figure 3.2:** Examples of synthetic head implant designs with cranial implants (in blue) and coils of various sizes and shapes (in yellow).

**Thoracic region:** Thorax implants show the most diversity with spine fixation implants, lumbar disk inserted between the vertebrae or complete shoulder prosthesis (see Figure 3.3). Plates were also designed and placed on the backbone, scapulae or coastal region and occasionally pacemakers were also



positioned in the upper chest region.

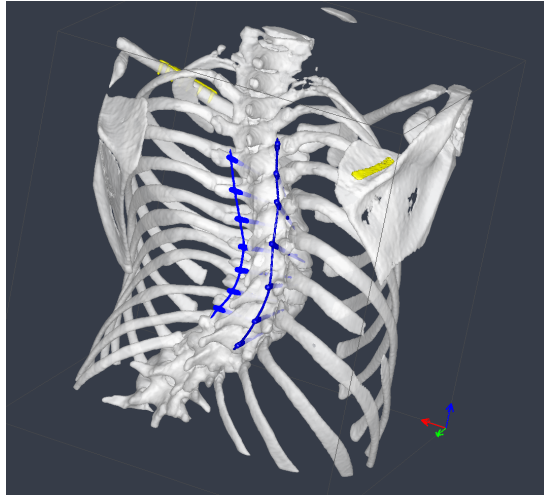


**Figure 3.3:** Example of thoracic implant designs designed with spine fixation (in blue) and plates (in yellow)

**Pelvic region:** Many pelvises were also included in CT-scans. Typical plates were designed with different meshing sizes and positioned on the ilium. Rods and screws were also added. As lumbar vertebrae are visible on most pelvic scans, lumbar disks and spine fixations were also designed (see Figure [3.4](#)).

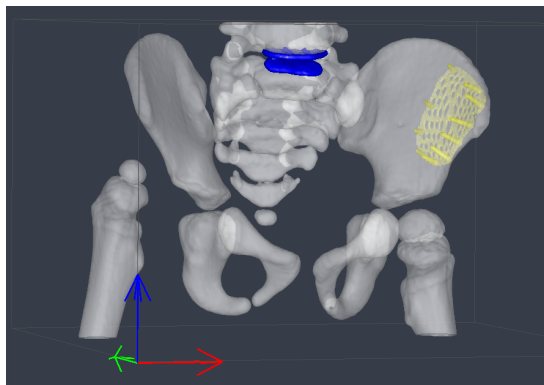
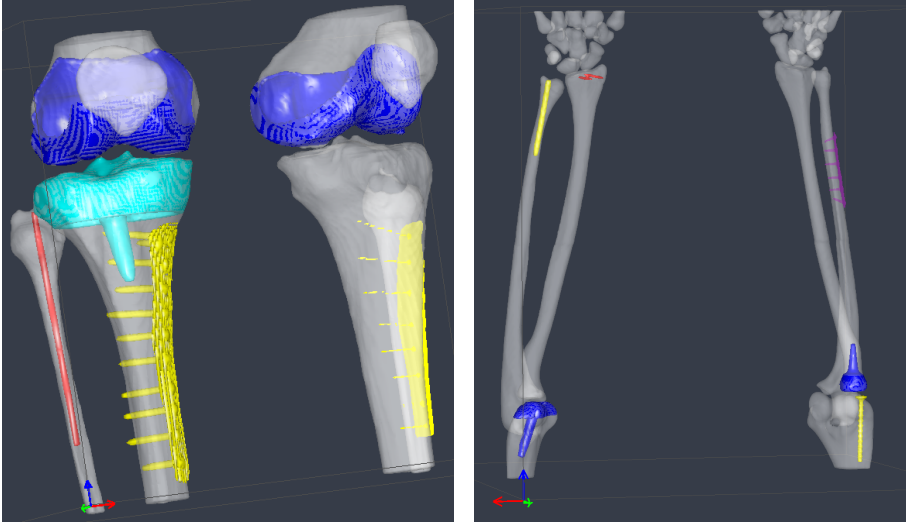


**Figure 3.4:** Example of pelvic implant designs with lumbar disk (in blue) and meshed plate (in yellow).

**Upper and lower limbs:** Upper and lower limbs being anatomically alike,

they encounter similar types of implants. Screws, bars and plates were thus placed on the long bones as normally done to heal fractures or provide a scaffold (see Figure 3.5). Joint prostheses (hips, knees, shoulders and wrist mostly) were also designed.



(a) Knee joint implants (blue) with plates (yellow) and rods (red). (b) Elbow joint implants (blue), plate (purple), rod and screw (yellow and red)

**Figure 3.5:** Example of implants designed for the superior and inferior regions.

### 3.4.2 Materials used for the synthetic implants

Seven types of metals were considered for the implants. Pure titanium, titanium alloy (Ti–6Al–4V), nitinol (Ni50–Ti50), 304 stainless steel (Fe–Cr18–Ni8), 316 stainless Steel (Fe–Cr16–Ni10–Mo2), cobalt alloy (Co–Cr30–Mo7–Ni1–Fe1–Mn1) and pure iron were used. They make up for most of the implants used clinically [20].

As the simulation required the densities of each metal, densities of pure metals were given in [22] and densities of the alloys were computed. For the density of the alloys ( $D_{alloy}$ ), it was calculated using the density of each of the individual components  $i$  ( $D_i$ ) with their relative mass fraction ( $X_i$ ). For that, let's consider the expression of the density of a material:

$$D_{mat} = \frac{m_{mat}}{V_{mat}} \quad (3.1)$$

With  $m_{mat}$  being the mass of the material (here the alloy) and  $V_{mat}$  its volume. Then, by taking the inverse of the expression [3.1](#), one obtains for an alloy made of two compounds ( $i \in [1,2]$ ):

$$\begin{aligned} \frac{1}{D_{alloy}} &= \frac{V_{alloy}}{m_{alloy}} \\ &= \frac{V_1}{m_{alloy}} + \frac{V_2}{m_{alloy}} \end{aligned} \quad (3.2)$$

Using [3.1](#) in [3.2](#) to replace  $V_i$  gives:

$$\begin{aligned} \frac{1}{D_{alloy}} &= \frac{m_1}{D_1 \cdot m_{alloy}} + \frac{m_2}{D_2 \cdot m_{alloy}} \\ &= \frac{X_1 \cdot m_{alloy}}{D_1 \cdot m_{alloy}} + \frac{X_2 \cdot m_{alloy}}{D_2 \cdot m_{alloy}} \\ &= \frac{X_1}{D_1} + \frac{X_2}{D_2} \end{aligned} \quad (3.3)$$

Where  $X_i$  is the mass fraction of the compound  $i$ .

For an alloy containing more than two compounds this formula can be extended. The densities for all the alloys used in the simulation were thus computed using the expression [3.3](#) above and listed in the table [3.1](#). The densities are then used later in order to generate synthetic artefacts.

### 3.4.3 Simulation of metal artefacts

Metal artefacts were simulated from the metal-free datasets with metal implants inserted. Metal artefacts generation mimicked a virtual axial scan of the metal-inserted datasets and was thus performed on the slice level. Each slice was virtually scanned twice. Once with the metal inserted in order to create artefacts and one without the metal. This double scanning allowed to properly extract regions of the scan with significant synthetic artefacts by comparing both scans. As the virtual scanning process alters the initial image quality and pixel intensity, poor results were obtained when trying to segment newly created artefacts by simply comparing the dataset before and after being virtually scanned.

For each slice of the volume the scanning process followed the flowchart [3.6](#) below. The pipeline mainly sticks to the method described in the paper by Mitsuki Sakamoto et al [\[4\]](#) which was inspired of Zhang et al.'s research

**Table 3.1:** Densities of pure metals [22] and metal alloys used for the synthetic metal implants.

Pure Metals		Density [ $\text{g/cm}^3$ ]
Aluminum		2,71
Chromium		7,19
Cobalt		8,75
Gold		19,32
Iron		7,85
Manganese		7,44
Molybdenum		10,19
Nickel		8,91
Platinum		21,4
Silver		10,49
Titanium		4,50
Vanadium		5,49
Metal alloy	Mixture	
Cobalt alloy	Co 60 Cr30 Mo7 Ni1 Fe1 Mn1	8,27
Nitinol	Ni50 Ti50	5,98
Stainless steel 304	Fe74 Cr18 Ni8	7,80
Stainless steel 316	Fe72 Cr16 Ni10 Mo 2	9,61
Titanium alloy	Ti90 Al6 V4	4,36

work [15]. Scattering was approximated as a constant scatter level according to [23] [24]. Scattering profiles usually contain low frequencies which explain the constant scattering level approximation. Scattered energy is usually described relatively to the primary beam energy as a ratio known as the scatter-to-primary ratio. This ratio was arbitrarily set to  $10^{-5}$  in the simulation.

In order to simulate polychromatic projections, the previous expression 2.3 was used. It simulates one polychromatic ray passing through an inhomogeneous material, in our case the patient's body. For one to use this formula, one must know the materials passed through by each X-ray. Consequently, pixels with bone-like ( $\mu_b$ ), water-like ( $\mu_w$ ) and metal-like ( $\mu_m$ ) attenuation properties were thresholded in order to segment the pixels into three distinct groups of known material characteristic. A double threshold technique was thus used so that pixels Hounsfield values above  $T_b$  were segmented as bone tissue pixels and pixels with HU values under  $T_w$  would be set as water-like tissues. The structures with HU values between  $T_b$  and  $T_w$  would be considered as a mixture of both tissues structures and thus a weighting function is used (3.4)

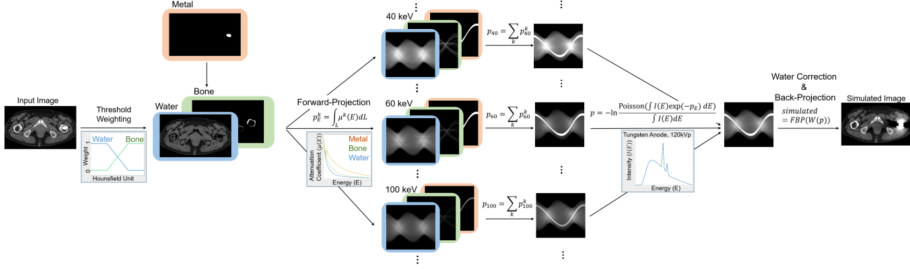


**Figure 3.6:** Overview of the synthetic artefact generation process inspired from Sakamoto et al [4] and Zhang et al.’s research work [15]. An additional scattering phenomenon was added after each single monochromatic projections to get more realistic artefacts. The flowchart above was designed by Sakamoto et al [4].

$$\omega(\mu) = \begin{cases} 0, & \mu \leq T_w \\ 1, & \mu \geq T_b \\ \frac{\mu - T_w}{T_b - T_w} & T_w < \mu < T_b \end{cases} \quad (3.4)$$

With  $\mu$  being the linear attenuation coefficient measured at the considered pixel. Then, for each pixel, the segmentation gives:

$$\mu_b = \omega(\mu) \mu \quad (3.5)$$

$$\mu_w = (1 - \omega(\mu)) \mu \quad (3.6)$$

The previous expression 2.3 for a polychromatic ray travelling through an object made of bone-like tissues 'b', water-like tissues 'w', metal 'm' becomes:

$$\begin{aligned} I &= \int I_0(E) e^{-\int_L \mu_b(x_b, E) + \mu_w(x_w, E) + \mu_m(x_m, E) dl} dE \\ &= \int I_0(E) e^{-\mu_b(x_b, E) l_b + \mu_w(x_w, E) l_w + \mu_m(x_m, E) l_m} dE \end{aligned} \quad (3.7)$$

The spectrum used for the virtual CT-scanner was modelled as combination of monochromatic X-ray beams with energies uniformly sampled every 1 keV from 1 keV to 140 keV. The spectrum was chosen among one of the eight spectra generated using an online tool provided by Siemens [25]. Seven spectra with different tube voltage potentials commonly used for clinical CT were first generated with tube potentials ranging from 80 kV to 140 kV with a 10 kV increments (see Figure 3.7). An additional spectrum was obtained using the most common tube potential (120 kV) with a 2.5 mm thick aluminum filter

as recommended in the Code of Federal Regulations (42 CFR 486.108).

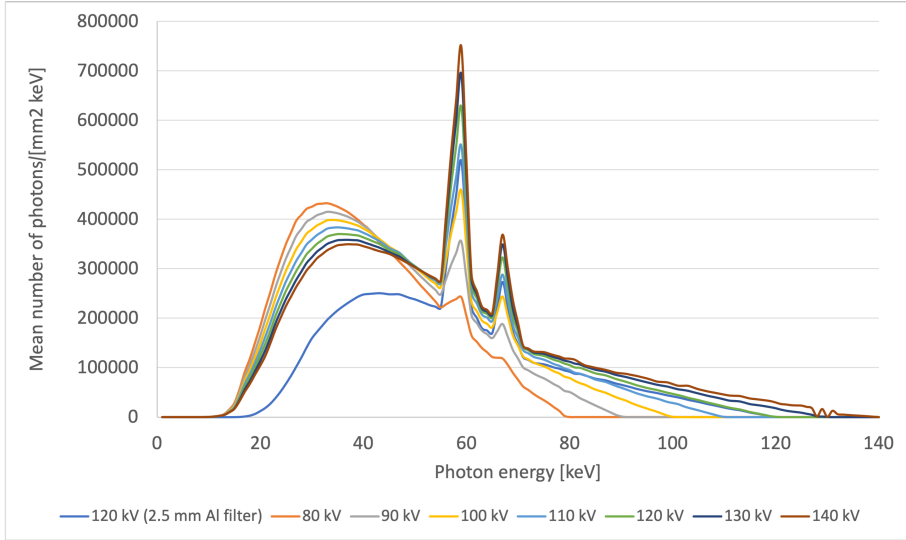


**Figure 3.7:** Spectra used to generate synthetic metal artefacts and obtained with Siemens online spectrum generator [25].

Each dataset was scanned using one of the spectra described above and illustrated in Figure 3.7. The integral from previous Equation 3.7 can thus be discretised as follows:

$$I = \sum_{k=1}^{E_{max}} I_0(E_k) e^{-\mu_b(E_k)l_b + \mu_w(E_k)l_w + \mu_m(E_k)l_m} \quad (3.8)$$

However, the linear attenuation coefficients are not convenient to use as they are dependent on the density of the material which is not always easy to assess [©Iowa State University Center for Nondestructive Evaluation (CNDE)]. For every material 'j', its linear attenuation coefficient can be written as the product of energy-dependent mass attenuation coefficient ' $m_j(E)$ ' (constant for a material) and the energy-independent density ' $\rho_j$ ' (unknown in our case) [8]

$$\mu_j(E) = m_j(E)\rho_j \quad (3.9)$$

Let's consider an arbitrary monochromatic energy  $E_0$ . Then the previous equation 3.9 gives:

$$\mu_j(E_0) = m_j(E_0)\rho_j \iff \rho_j = \frac{\mu_j(E_0)}{m_j(E_0)} \quad (3.10)$$

With mass attenuation coefficient being strictly positive constants. The initial equation [3.9](#) can then be rewritten as:

$$\mu_j(E) = m_j(E)\rho_j = m_j(E)\frac{\mu_j(E_0)}{m_j(E_0)} \quad (3.11)$$

Adding this relation to Equation [3.8](#) gives:

$$I = \sum_{k=1}^{120} I_0(E_k) e^{-m_b(E_k)\frac{\mu_b(E_0)}{m_b(E_0)}l_b + m_w(E_k)\frac{\mu_w(E_0)}{m_w(E_0)}l_w + m_m(E_k)\frac{\mu_m(E_0)}{m_m(E_0)}l_m} \quad (3.12)$$

The projections values were then computed using Equation [2.5](#) derived from Equation [2.4](#)

Mass attenuation coefficients were obtained from the XCOM database [\[26\]](#) using the materials formula from table [3.1](#). Both scattering and photoelectric absorption effects were taken into account when generating the mass attenuation coefficients listed in the table [7.3](#). Bone attenuation coefficient values were based on standard cortical bone composition given in the ICRU report 44 [\[27\]](#). Water mass attenuation coefficients were simply obtained using the H<sub>2</sub>O chemical formula. The monochromatic mass attenuation coefficient were obtained using the equivalent monochromatic energy of the spectrum [3.2](#) estimated as the mean energy of the spectrum.

Finally, a water beam-hardening correction method was implemented based on Herman's paper [\[28\]](#).

**Table 3.2:** Equivalent monochromatic energies given for each spectrum displayed on the plot [3.7](#) and generated with Siemens online generator [\[25\]](#).

	80 kV	90 kV	100 kV	110 kV	120 kV	130 kV	140 kV	120 kV 2.5mm Al filter
Equivalent monochromatic energy [keV]	40.8	43.9	46.7	49.2	51.5	53.7	55.5	57.6

The previous equations enabled to virtually model the attenuation of a single polychromatic X-ray along a straight path. To mimic a real beam, multiple X-rays were then simulated similarly to a conventional CT-scan. The simulator should theoretically rely on a typical fan-beam scanner with one source and multiple divergent X-rays paths. However, the in-built MATLAB function *fanbeam* which mimics fan-beam based FP does not support GPU. To reduce computation time, the in-built *radon* function was used instead as it is compatible with GPU. More details about radon and fanbeam projections are given in the section [3.4.4](#).

Once projected and stored as a sinogram, each slice was then reconstructed using FBP. Here again the *iradon* function was used instead of *ifanbeam* for similar reasons as before. Five different filters (Ram-Lak, Shepp-Logan, Cosine, Hamming and Hann) were used interchangeably for the filtering to avoid potential bias.

### 3.4.4 Fanbeam and radon projections

In most CT, the projection data from one slice is collected using divergent beams known as fanbeams [29]. From the unique source  $S$  is emitted multiple divergent X-rays that travel through the studied object before reaching sensors opposing the source. The source and the sensors are then rotated from a certain angle  $\theta$  and another projection is performed. The same process is repeated until the complete profile of the object contained in the slice has been collected.

Radon-based projections are different as data is collected from multiple parallel beams originating from different sources. For the virtual scanner, each path or beam is 1 pixel spaced apart in a given direction. Similarly to the fan-beam configuration, the sensors are placed in opposition to the sources with the object to scan in the middle. Once again, the sources and sensors are rotated and more projections are collected. This process is repeated until the object has been fully scanned within the slice. A half turn would be sufficient here to obtain the complete profile of the object as the attenuation values would be similar for a rotation of  $180^\circ$ . Indeed, the sources and sensors would simply flip positions but the paths would be the same. Both radon and fanbeam transforms are illustrated in Figure 3.8.

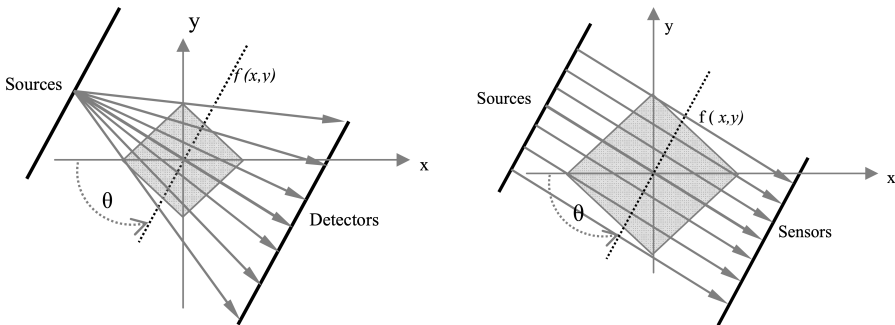


**Figure 3.8:** Illustrations of both fanbeam (Left) and radon (Right) projection methods. Illustrations were originally from Naser et al. [29]

The inverse transforms named *ifanbeam* and *iradon* enable the opposite process as they reconstruct images from projections obtained with fan-beam



and radon.

The fanbeam geometry is mostly used in real CT reconstruction since it enables a rapid and more efficient collection of projections as only one source is needed [29], [30]. However, for virtual scanning on MATLAB, these assets are less relevant. The number of sources that can be a problem for real scans is not when done virtually. Moreover both radon and iradon built-in functions support GPU computation contrary to fanbeam and ifanbeam. In terms of reconstruction, very little difference was seen between both geometries when similar parameters were chosen. A Shepp-Logan phantom, commonly used to model a human head, was used to validate the previous assumption. The background of the phantom was set to -1000 which is the usual value for air. Other portions of the phantom were given HU values close to real soft tissue and hard tissue [31] with HU values ranging from -200 to 700 HU . The phantom was then virtually scanned with each method using the same X-ray spectrum. Scanning parameters for each method were given similar values when possible. The output images were compared by taking the absolute difference of the pixel values. Another pair of scans was performed with a metal-like portion added in the middle of the head. The HU value for the simulated metal was chosen in line with real clinical metal projections ( $HU_{metal} = 8000$  HU) [32]. Both comparisons (see Figure 3.10) clearly showed that HU differences are inferior at 95% to 22 HU. This applies regardless of metal in the FOV.

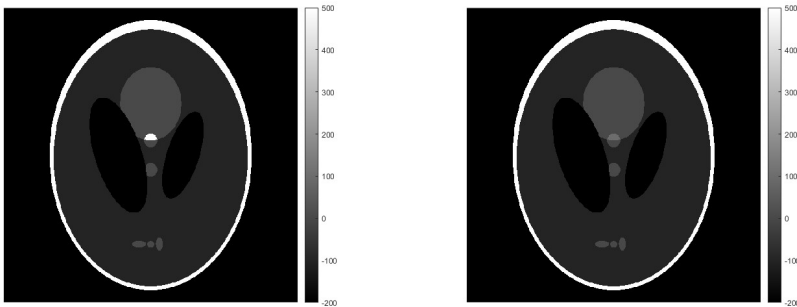


**Figure 3.9:** Shepp-Logan phantom used to test both reconstruction methods (Radon and Fanbeam). A metal-like portion was added (Left) in the middle of the original phantom geometry (Right).

This difference occurs mainly because of the noisy nature of FBP and the potential rounding errors. This is exhibited by many bright dots on the subtracted images (see Figure 3.11). However, the strongest differences occur at

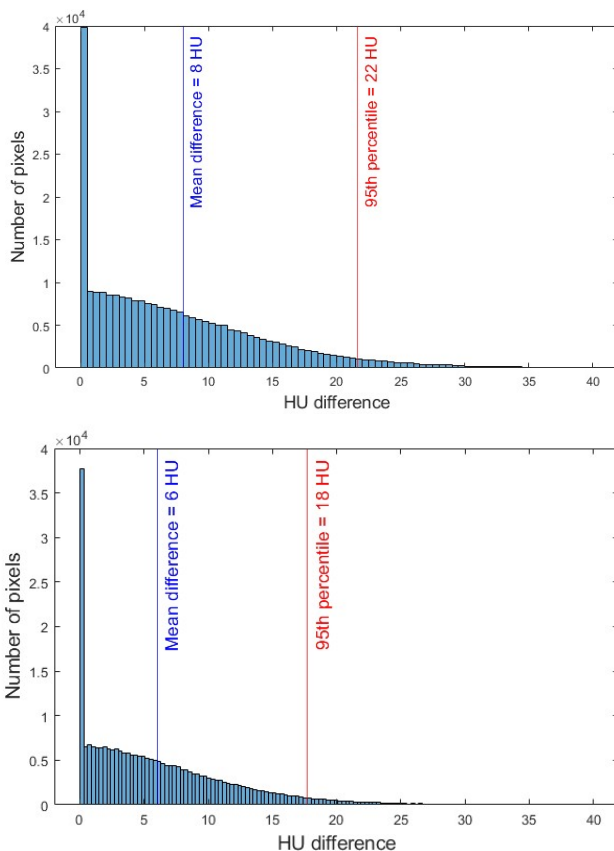


**Figure 3.10:** Histograms obtained after comparing virtual Shepp Logan phantom reconstruction obtained with both methods (Radon and Fanbeam) with metal (Up) and without (Down).

the edges of the bone-like tissues. It is likely because this region is at the intersection of two kinds of very different tissues. In the end, both methods provide very similar images with a mean pixel intensity difference inferior to 8 HU).

Finally, in terms of metal artefacts, one can notice that they produce visually similar artefacts (see Figure 3.12). Even on the subtracted image with metal, no noticeable difference was observed around the metal. It was mainly the air region that was a bit noisier compared to the subtracted image without metal.

Both method speeds were assessed using a  $512 \times 512 \times 10$  volume made of repeated Shepp-Logan phantom slices. Very similar arguments were used for

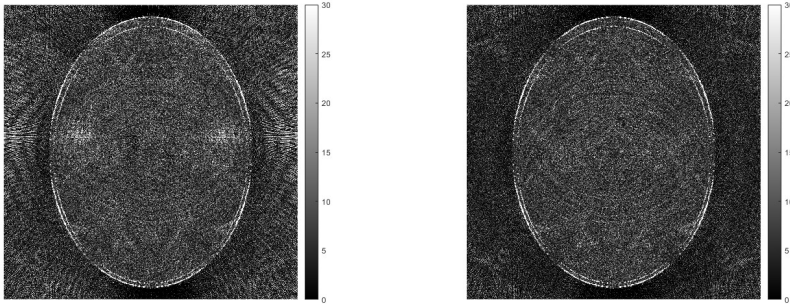


**Figure 3.11:** Images obtained after subtracting phantom reconstructions obtained with both methods (Radon and Fanbeam) with metal (Left) and without (Right).

both methods and similar simulation properties were used. In the end, the fanbeam method was 35 % faster than the radon one (see Table 3.3). The radon reconstruction was thus used in this thesis. Since the difference between both reconstruction techniques was small it was deemed that using radon transforms would not create bias for the DL network.

**Table 3.3:** Speed comparison between both radon and fanbeam reconstruction methods for a volume of 512 x 512 x 10.

<b>Radon speed (s)</b>	1.940	<b>Iranon speed (s)</b>	0.187	<b>Total speed (s)</b>	2.127
<b>Fanbeam speed (s)</b>	2.383	<b>Ifanbeam speed (s)</b>	0.904	<b>Total speed (s)</b>	3.287

## 3.5 Architecture and training of the U-Net

### 3.5.1 Architecture of the network

The same U-Net network structure and hyper parameters as in the existing algorithm [33] were used in this thesis. The U-net is convolutional neural network frequently used in medical image segmentations.

The input volume is divided into three orthogonal stacks of 2D images. Each slice is then divided in 128x128 patches used as an input for the U-Net network. For each orthogonal orientation, one 3D binary segmentation is output. A single 3D volume is then obtained using voxel-wise voting. The complete process is illustrated in Figure 3.13. Image adopted from Medviso in-house regulatory documentation.

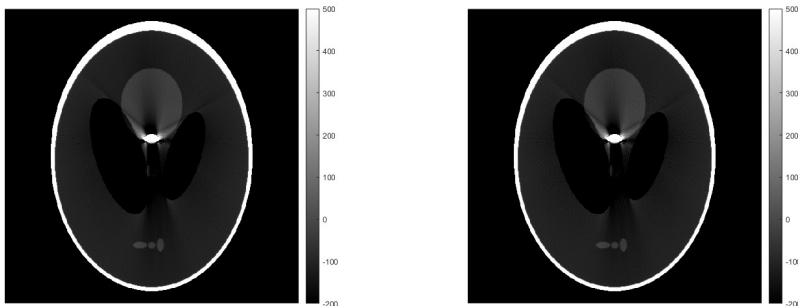


**Figure 3.12:** Reconstructed images from original Shepp Logan phantom using Radon (Up) and Fan-beam (Down) in the presence of metal.

### 3.5.2 Generation of label classes

A total of 3 label classes were generated and input in the training.

**Bone:** A bone class was generated to cover all pixels in the CT-scans containing bone. Bone segmentation was performed using the current DL bone-segmentation tool. For each dataset, careful manual editing was also performed to ensure as accurate segmentation as possible. Data sets with metal artefacts required significant manual processing. Segmentation was performed by myself and reviewed by Prof. Einar Heiberg, an experienced observer.

**Metal:** All the synthetic and real implants were assigned a common label that could then be used to generate artefacts. The labelling for the real metal parts was obtained from the CT-images using a threshold technique. The threshold was chosen so that the metal would be extracted without any bone. A slight smoothing inferior to 1 mm was applied for a better rendering. For very dense metals, artefacts were also extracted with the threshold and extra manual processing was then performed to obtain a proper label for the metal.

**Separator:** An extra separator class was created by a closing operation of the bone class subtracted by the bone segmentation. This class can then in a post-processing step be used to force separation of bones, for instance in joints.

In addition to the first three classes, an artefact-mask containing regions affected by metal artefacts was created. This mask was essentially used to enhance patches selection and favour patches with strong artefacts that could potentially lead to an incorrect segmentation. For the metal-inserted datasets, this

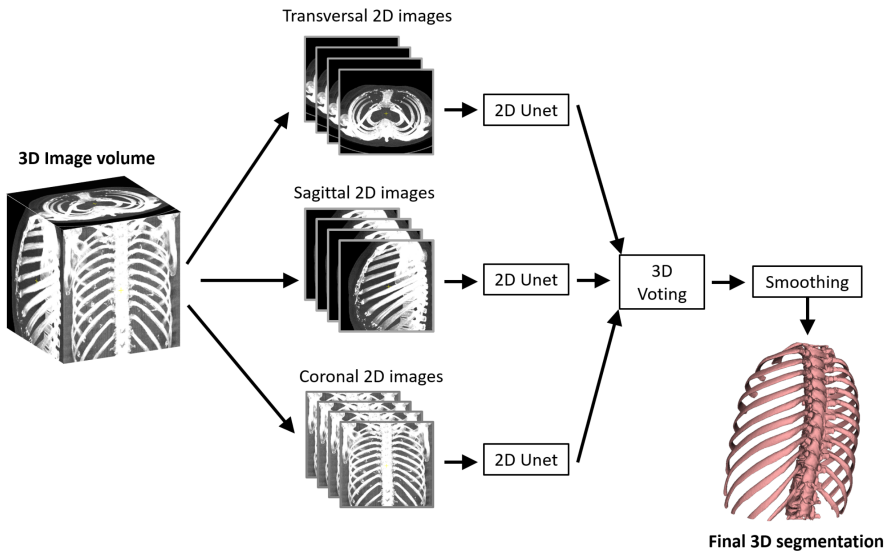


**Figure 3.13:** Overview of the bone segmentation algorithm developed by Medviso for their Segment 3DPrint software.

class was created by comparing each slice with and without synthetic artefacts. Indeed, the CT-volume was first virtually scanned once without any metal and then a second time with the associated metal parts. Doing so, provided better results as it ensured that both volumes were very identical in terms of HU values except for the regions where artefacts were created. Then the absolute difference between both volumes was computed and a threshold applied. The threshold was set to 150 HU by visual assessment of the artefacts. Indeed, artefacts under 150 HU were not strong enough to eventually cause segmentation errors. For datasets with real metal, the initial segmentation tool was used in the slices containing a metal part. The output object was then compared with the bone label and the difference was kept as to create an artefact mask. Minimal manual adjustments were performed to ensure that only artefacts were taken into account and not potential other artefacts.

### 3.5.3 Data augmentation

To improve the training, data was augmented as it was known to improve training performance [34].

First, each metal-free dataset was virtually scanned multiple times using random combination of the synthetic implants designed beforehand. For each simulation, simulation parameters (X-ray spectrum, implant material, Poisson noise, scatter noise and filter) were also modified randomly to generated com-

pletely different artefacts and thus provide a very rich input for the training of the DL network. This first augmentation process enabled creating complex and rich training data from each individual dataset. Datasets exhibiting real metal artefacts were also virtually scanned with the simulator but with an empty metal-mask. This way, no additional artefacts were created but the global pixel intensity was still slightly modified depending on the spectrum and noise level used for the simulation.

Datasets were then randomly rotated in 3D and thereafter 2D augmentations in patches of slices in all three orthogonal directions were performed. Patches were affected with geometric transformations (flipping, rotation, scaling, intensity and contrast and mirroring). Table 3.4 described each augmentation with its corresponding probability.

The data augmentation was changed before each new epoch so that the same patches would not be used twice which reduces the risk for potential overfitting.

**Table 3.4:** Table of the augmentations used with corresponding probability of occurrence (middle column) and distribution for augmentation parameter.

Augmentation	Probability	Distribution	Unit
Rotation	25 %	U(-45, 45)	Degrees
Scaling	100 %	U(0.6, 1.4)	Factor
Translation	25 %	U(-64,64)	Pixels
Mirroring horisontally	50%	-	-
Mirroring vertically	50%	-	-
Transpose	50%	-	-
White noise	20%	U(0, 15%)	Of intensity range
Brightness	25 %	U(-100, 100)	HU
Contrast	25 %	U(0.7, 1.3)	Factor
Gaussian blurring	25 %	{3, 5,7}	Filter size in pixels
Rescan dataset with metal	75 %	-	-
Keep metal shape	75 %	-	-
Implant material	100 %	U(1,7)	Density [g/cm <sup>3</sup> ] and mass attenuation coefficient [cm <sup>2</sup> /g]
Poisson Noise	100 %	U(11, 14)	Factor of 10
Filter option	100 %	U(1,5)	Filter type: Ram Lak, Shepp-Logan, Cosine, Hamming, Hann

### 3.6 Training

Datasets were partitioned into training data and test data (see Figures 7.1 and 7.2). 50 datasets were kept for the training and 25 for the test. Datasets were carefully sorted in order to keep as much diversity as possible in each partition. For the training data it is important to train the DL network on very divers datasets to build up its robustness. The test data was even more crucial as it is

meticulously inspected by the FDA in order to approve the commercialisation of the DL network. Significant variety in age, acquisition dates, anatomical regions scanned, disease and scanner brands was thus crucial for this partition. Finally, datasets exhibiting knees were kept strictly in the test data in order to assess the DL network ability to segment bones from unknown anatomical regions. Once the datasets partitioned, the training process was designed and optimised.

In order to generate a computationally effective training environment we developed two independent processes. One process creates augmented training patches and another process performs the training.

Patches were generated by the function *patchgenerator(S)* where *S* is the argument containing all configurations for the augmentation and training. Each dataset from the *train data* folder were augmented continuously. The patches generated were then saved in the *patches* folder with the corresponding label patches. Simultaneously, as soon as 80 000 patches were stored in the *patches* folder, one epoch of the training would start on the second process. 80 000 patches were chosen as it seemed to be a good amount of patches when used to train the previous DL bone-segmentation tool. The patches used in the epoch were then deleted from the original folder to avoid using them twice. This bucket-leak system allowed to decrease computational time as the two processes could run on different CPU's and also the training did not have to wait for augmentation to finish to start next epoch.

### 3.7 Metal artefacts assessment

In order to assess the synthetic artefacts generated with the previous pipeline (see Figure 3.6), a phantom experiment was carried out. A anthropomorphic forearm phantom was used to reproduce human tissues with bone-like structures. Then, different metal parts with known composition were taped on the phantom at various locations (see Figure 3.14). A gold ring was placed on the index, a platinum coil on the metacarpals, two stainless steel plates with a screw around the wrist and one spanner made of a cobalt alloy on the forearm.

The phantom was then scanned three times using a 120 kV tube voltage, as commonly done for clinical cases. Two scans with a standard CTDIvol dose around 4.5 mGy were performed, with and without metal. An extra scan with metal was done using a high mAs setting to get a very high dose scan.

In order to assess the generated artefacts, three slices from the standard dose scan displaying metal parts were chosen for thorough analysis. Each slice

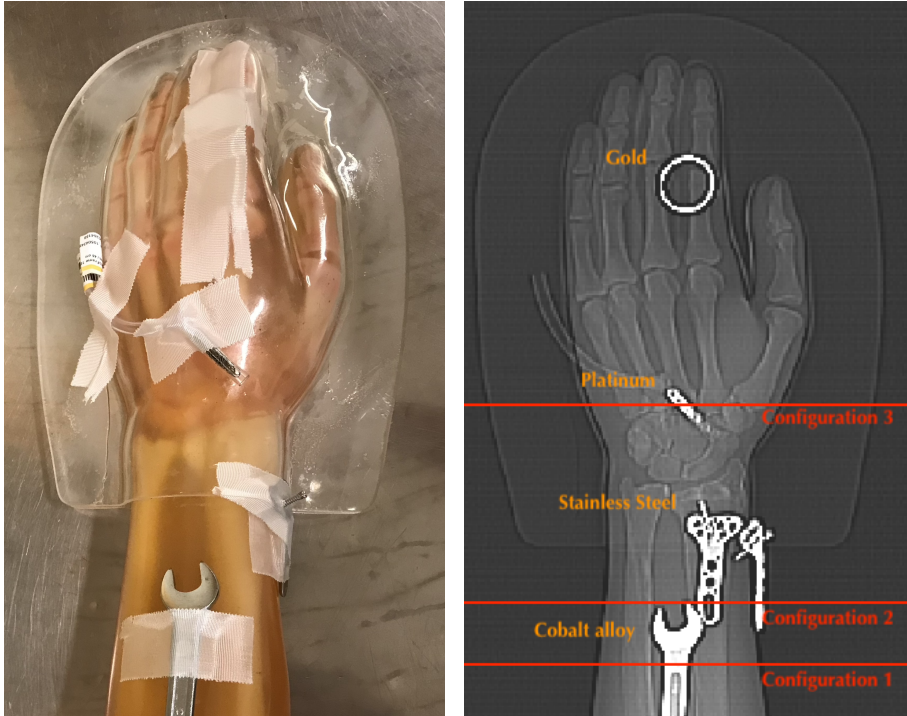


**Figure 3.14:** Anthropomorphic forearm phantom used for the assessment of the synthetic metal artefacts. Metal parts (indicated with orange lettering) were taped to the phantom and can be observed in the standard photo of the phantom (Left) and on the 2D X-ray image (Right). All three configurations considered in the analysis are shown on the X-ray image in red.

was selected based on the metal configuration. Metal configurations leading to complex and strong metal artefacts were chosen. The slices positions are shown on the 2D X-ray image (see Figure 3.14). A first configuration containing a significant piece of cobalt alloy was chosen. A second configuration showing multiple pieces of stainless steel and cobalt alloy parts was also retained for analysis. The complexity of the artefacts generated by the interactions between all individual metal parts was essential to simulate in order to test the synthetic artefacts. Finally, a configuration displaying a very dense metal was used for comparison as well. The slice contained platinum from the coils. Matching slices from the scan without metal parts were used for the simulation of the synthetic artefacts.

However, an additional 2D registration step was needed to ensure a perfect superposition of the slices without metal on the slices with metal parts.



Indeed, the phantom was potentially moved during the scanning process and the reconstruction field of view was placed manually for each single leading to slight misalignment (see figure [3.15](#)). Unwanted rotation and translations were therefore corrected using a rigid registration. For each configuration, the geometric transformations were estimated using the imbuilt MATLAB functions *imregtform*. The transformations were then applied to the CT slice without metal using *imwarp*.

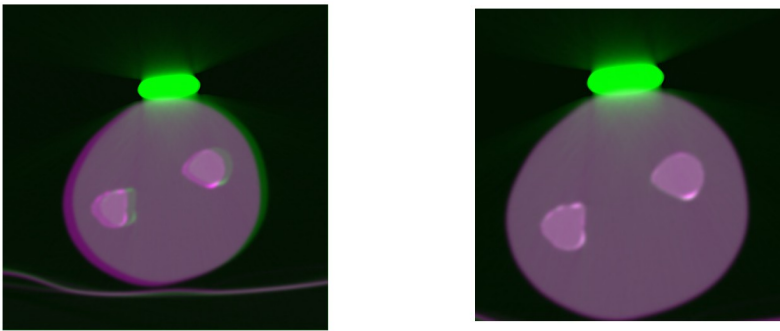


**Figure 3.15:** Misaligned slices (Left) registered with rigid transformations. The aligned slices were then cropped (Right) with dimension 401x401.

Thereafter, scans were cropped (401x401) in order to remove the borders and keep the metal artefacts and the whole phantom in the image. Metal shapes were then extracted from the slices with metal parts to generate synthetics artefacts on the slices originally not displaying metal. As the HU values of the metal is very high compared to soft and hard tissues (see Histogram in Figure [3.16](#)) a simple threshold around 3000 HU was used to segment metal from all three configurations. However, this threshold-based segmentation performed poorly with gold and platinum metals. It was impossible to obtain a proper segmentation of the ring as gold creates major artefacts that result in pixel values over 3071 HU outside of the metal. But the 12 bit reconstruction, common for many scanners, allows only pixel values ranging from -1024 up to 3071. It is then impossible to make a distinction between pixels displaying real metal or just strong artefacts around the metal part as a higher threshold value can not be chosen to make the distinction. When thresholding the metal, artefacts were also segmented resulting in a completely inaccurate shape. One attempt to segment the ring and the coils from the high dose scan with less artefacts was performed. Still, little improvement has been noticed (see Figure [3.17](#)). Concerning the coils, it was impossible to separate the threads forming the

coils. Instead, it was thresholded as one significant piece of platinum.

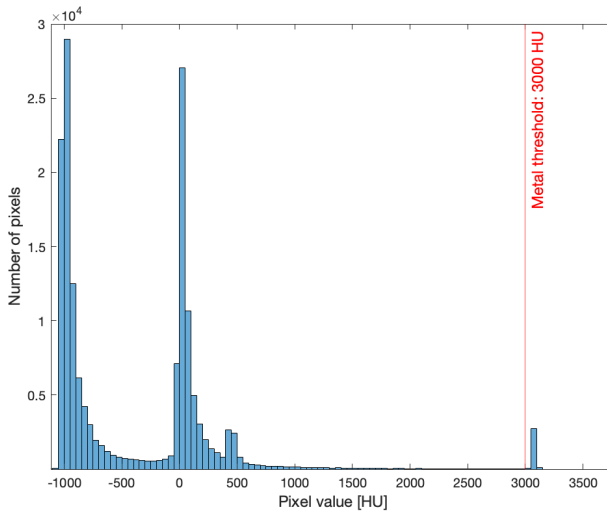


**Figure 3.16:** Histogram computed from the first configuration on the CT slice with metal. A threshold around 3000 HU just before the metal peak was kept to segment all metal parts from the slice.

Once the metal shapes were extracted, spectrum and metal properties were chosen according to the experiment settings to generate synthetic artefacts. A 120 kV spectrum filtered with a 2.5 mm aluminum sheet was used for the simulations. The resulting images were blurred with a Gaussian filter as they were initially too sharp compared to the real scans displaying metal. A standard deviation of 2 was chosen for the filter based on visual inspection.

Following the generation of synthetic artefacts for each three configurations, analysis was performed to compare slices with synthetic and real artefacts. First, a visual assessment was carried out to describe the general shape of the artefacts and their relation to the underlying physical causes. A quantitative study followed using all three slices for each configuration (slice with real artefacts, with synthetic artefacts and without artefacts). The computation of the metrics is described in the figure [3.18](#) below.

Ten-pixel wide bands (horizontal and vertical) crossing the center of each slice were extracted as shown in the first step described in Figure [3.18](#). Each band was averaged along its width in order to get general pixel value fluctuation along both perpendicular axes. The averaged fluctuations should reflect

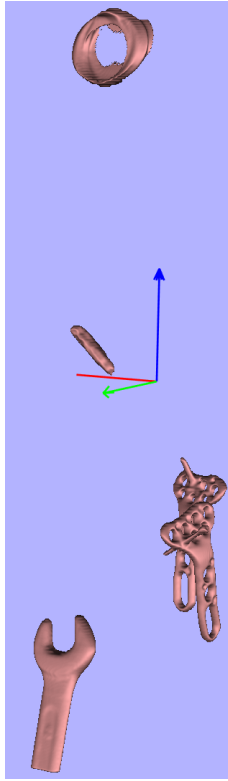


**Figure 3.17:** Thresholded metal from the high dose scan with less artefacts. Both the gold ring and the coils segmentations were inaccurate because of strong artefacts.

the presence of artefacts (both real and synthetic) in the overall image. An additional metric for each band was extracted to compare both vertical and horizontal fluctuations separately. For that, the mean absolute difference was computed to compare the slice with real metal and both slices before and after generating synthetic artefacts.

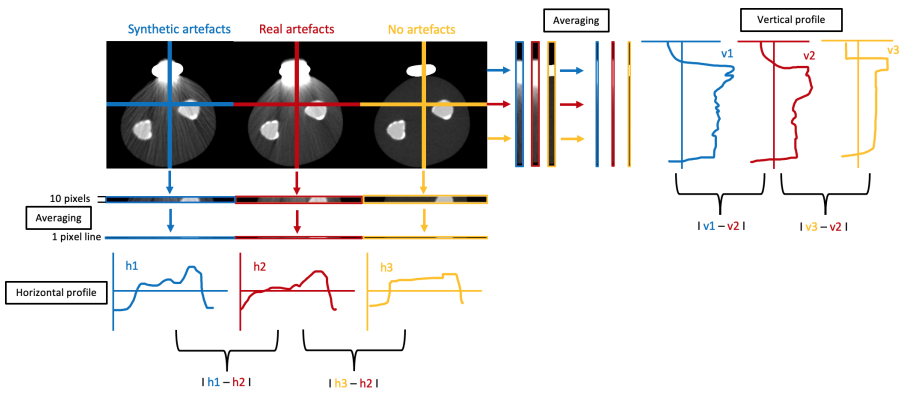


**Figure 3.18:** Description of the quantitative analysis process.

## 4. Results

In this chapter, qualitative and quantitative evaluation of the synthetic artefacts is presented.

### 4.1 Visual assessment of simulated artefacts

Synthetic and real artefacts from all three slices are displayed on the figure [4.1](#) below:

Both real and simulated artefacts in Figure [4.1](#) are similar. Thin dark and bright streaks originating from the metal part made of cobalt alloy are visible on both types of artefacts and look sensibly similar as direction of the streaks is sensibly the same. Moreover, wider dark streaks are also visible in directions where attenuation is the most significant, i.e between the brightest (and thus most attenuating) parts of the bones and the metal alloy. This phenomenon resulting from beam hardening is more obvious for configuration b) (slices in the middle row of Figure [4.1](#)). There, multiple dark streaks connected all individual metal parts are visible. This shadowing effect is clearly more predominant in the synthetic artefacts. Instead of stainless steel, titanium that exhibits weaker attenuation, was simulated and gave better results with softer artefacts. For the third configuration, this is where the synthetic artefacts are the least similar to the real ones. Noise is significant with sharp thin streaks. Shadowing induced because of beam hardening is more present in the synthetic slice. Finally, the white halo emanating from the metal parts is completely different between the two slices.

Quantitative analysis was also performed on the previously described slices.

### 4.2 Quantitative evaluation of simulated artefacts

As expected from the visual inspection, for the last configuration, the synthetic artefacts were very different from the real ones. When looking at the horizontal fluctuations (upper plot from Figure [4.4](#)), the slice before generating the artefacts and the slice with real artefacts are more similar. The thin sharp streaks from the real artefact slice have probably faded because of the averaging process. In general, the synthetic artefact cast a global shadow over the

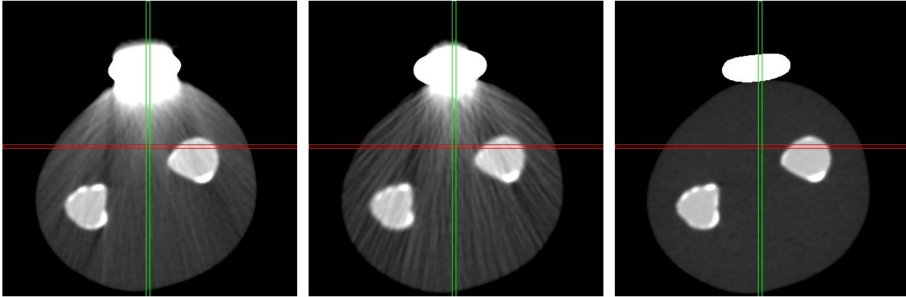
slice resulting in overall lower pixel intensity. This difference was well captured by the average fluctuation metric (Table 4.1). The horizontal metric is twice bigger for the slice after generation of artefacts. Such result implies that the slice before generating the synthetic artefacts experience a pixel intensity fluctuation closer to the slice with real artefacts.

For the second configuration, the pixel intensity fluctuations (both vertically and horizontally) exhibit very similar evolution between real and synthetic artefacts slices. Globally, the synthetic artefacts seem more substantial. It is clearly noticeable around peak values both on the horizontal direction (at the positions 200, 245, 255 ad 310 on the X axis) and vertical view (around 75, 150 and 235 on the Y axis). Here, the metrics from Table 4.1 point in the same direction with very little absolute difference inferior to 20 HU along the vertical direction.

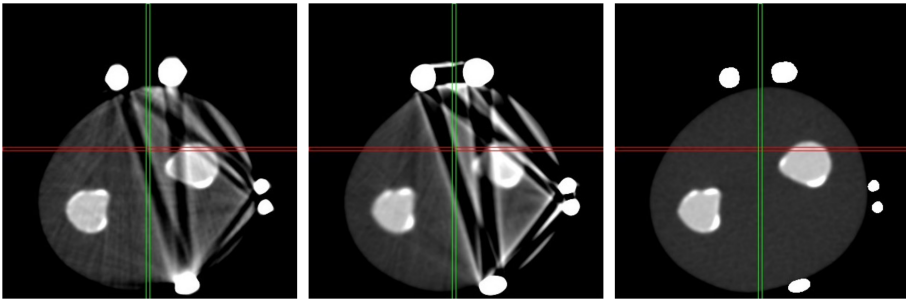
Finally, the first configuration with only the cobalt alloy, is the one where the synthetic artefacts are the closest to the real ones. Despite being slightly less intense, the evolution of the average pixel intensity along the horizontal and vertical band follow almost perfectly the ones from the pixels containing real artefacts. It is important to notice, on the vertical view, how the average pixel intensity is curved around the region where lays the metal. There, it is easy to notice that the pixel values saturate at 3071 because of 12 bit reconstruction, mentioned previously.

**Table 4.1:** Metrics obtained for all three configurations and band orientations (horizontal and vertical). The absolute difference was used to compare average pixel fluctuations.

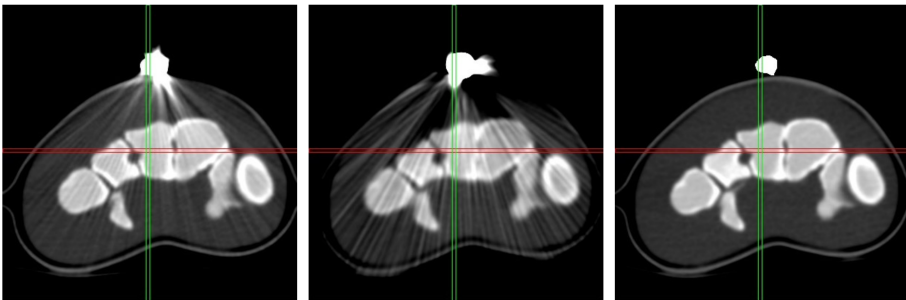
	<b>Band Direction</b>	<b>Simulated/Real</b>	<b>No metal/Real</b>
<b>Configuration 1</b>	Horizontal	31.6	80.4
	Vertical	32.3	318.9
<b>Configuration 2</b>	Horizontal	59.3	71.9
	Vertical	19.3	61.0
<b>Configuration 3</b>	Horizontal	61.9	30.6
	Vertical	78.7	141.9



(a) Configuration 1: Cobalt alloy spanner



(b) Configuration 2: Cobalt alloy and Stainless Steel



(c) Configuration 1: Platinum coils

**Figure 4.1:** For each three configurations are shown the slices showing real artefacts (Left column), after generating synthetic artefacts (middle column) and before (Right column).

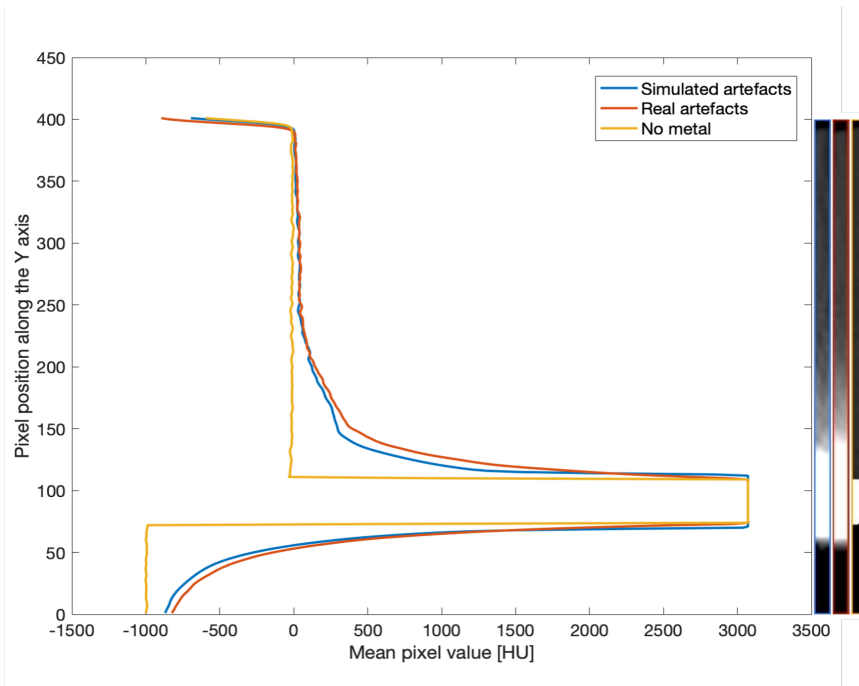
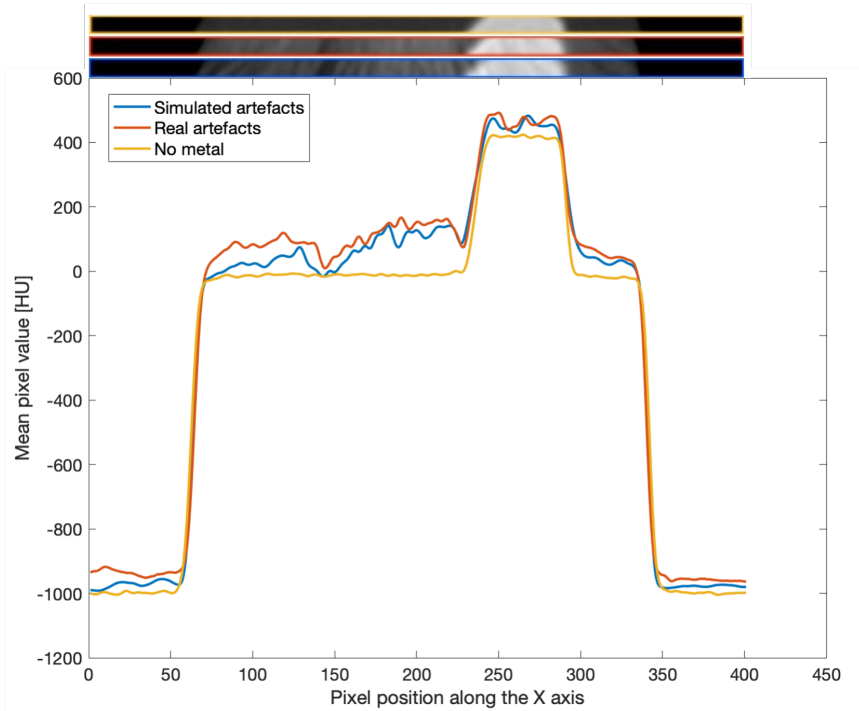


**Figure 4.2:** Average pixel intensity fluctuation recorded in the horizontal 10-pixel wide band (Up) and vertical (Down) for the first configuration with only cobalt alloy in the slice.



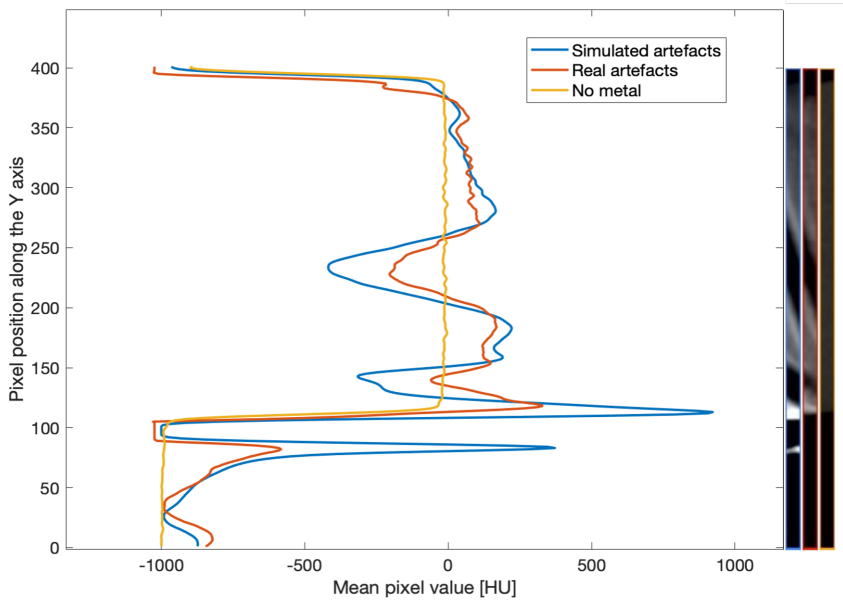
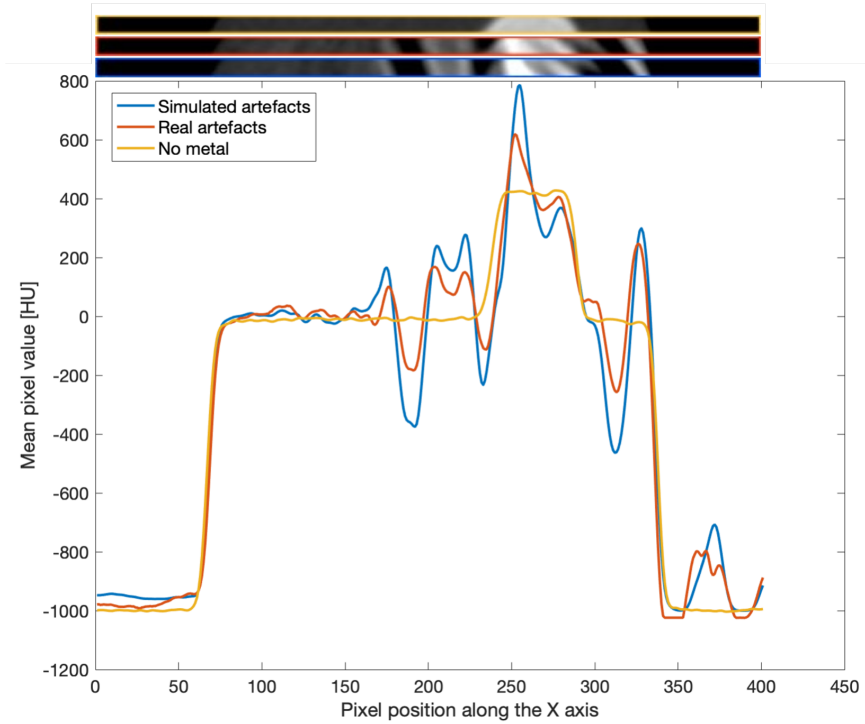


**Figure 4.3:** Average pixel intensity fluctuation recorded in the horizontal 10-pixel wide band (Up) and vertical (Down) for the second configuration with multiple stainless steel parts and one cobalt alloy metal.

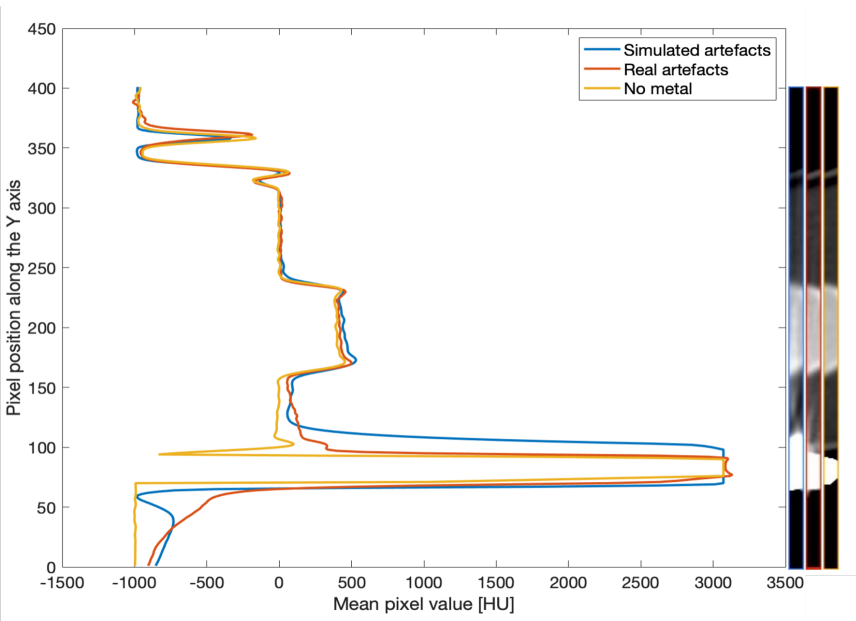
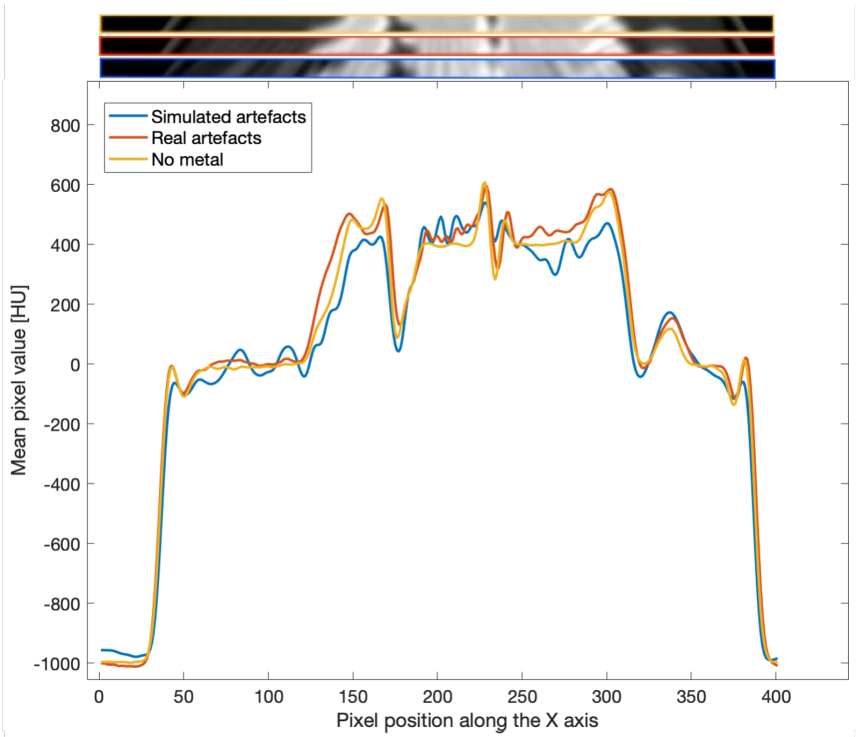


**Figure 4.4:** Average pixel intensity fluctuation recorded in the horizontal 10-pixel wide band (Up) and vertical (Down) for the third configuration with the platinum coils.

## 5. Discussion

A promising metal artefact simulator was developed capable of reproducing multiple physical phenomena constituting the core for the generation of metal artefact. Beam hardening, scatter, Poisson noise and photon starvation were all represented in the simulated artefacts at various intensities. Globally, beam hardening seemed to dominate with very dark bands along directions where the attenuation is the most significant (see Figure 4.1). Moreover, the simulator has successfully be able to generate artefacts even in complex cases with multiple metal parts. However, the synthetic artefacts were stronger in configuration c) also because of the initial metal mask used for the simulation. If it has been possible to obtain the real shape of the coils (made of multiple threads), the simulation would have undoubtedly been different. Indeed, it was thresholded as a solid block of platinum that was used as the metal mask for the simulator leading to stronger synthetic artefacts. Overall, despite few differences, the synthetic artefacts seemed useful to create a database with complex and divers artefacts that could be used to train a U-Net.

### 5.1 Limitations

Plates placed on the scapulae were particularly interesting as the bone is very thin in this region leading to poor DL bone-segmentation. Indeed, even without metal artefact, the initial DL bone-segmentation tool failed to properly segment the scapulae on multiple cases (see Figure 5.1). With metal artefacts, this phenomenon is even more accentuated (see Figure 5.1) which in the end requires additional manual processing if this region is of interest.

In addition, the generation of patches and especially the simulation of metal artefacts is very time-demanding. Indeed, for a dataset of dimension  $n^3$ , the current simulation is  $O(n^3)$  as the simulation is performed twice to obtain the artefact-mask. Implementing a 3D version of the radon and iradon transform in  $O(n \log(n))$  based on Amir Averbuch and Yoel Shkolnisky' paper [35] could decrease simulation time. Moreover, finding another way to obtain a mask artefact without simulating twice the whole dataset could be advantageous.

It would also be very interesting to change how patches are chosen. So

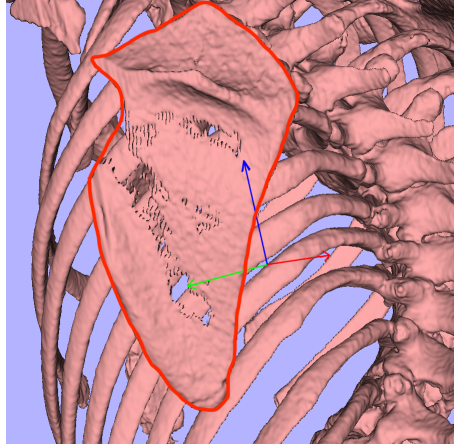


**Figure 5.1:** Example of poor scapulae segmentation (delineated in red) using the initial DL bone segmentation tool.

far patches generation is based on how much bone or artefact is shown on the patch. However, to make it better, it could learn from its own mistake by choosing patches where the previous network wrongly labelled regions. For each dataset, the last available network would be used to output a segmentation of the bone and would then be compared to the ground truth segmentation. A mask would then be created based on differences between those two segmentations. The mask would then be used to select patches to keep for the training. Doing so would make the network in a more direct way learn from its own mistakes as it will get more training on the data where it fails. However, it happens that within the FOV stand various objects (table, right or left ruler) with attenuating properties similar to bone. When using the DL bone-segmentation tool it happens that those objects end up being segmented as well. A way to overcome this issue, would be to have a second ground truth segmentation with unwanted objects. Whenever the network would be used to obtain the mask, the second ground truth would be used to remove these unwanted objects.

## 5.2 Future work

Considering the time allocated for this project, it has not been feasible to train and test the artefact-robust bone-segmentation tool. Comparing the current DL bone-segmentation tool and one trained using the metal artefact augmentation presented in this thesis could be of great interest. For datasets with metal artefacts, both networks should be tested on regions where the artefacts are the

strongest. In the absence of artefacts, it is also important that the artefact-robust bone segmentation tool be as accurate as the current one. Finally, depending on the artefact-robust DL bone-segmentation tool performance, the option to use 3-channel patches should be investigated using the already implemented MAR techniques (LI and BHC). However, for this network to work on datasets with real artefacts, it would require the user to first get the shape of all metals in the scan. Indeed, both LI and BHC require metal projections to reduce artefacts. A simple user-friendly interface could be added to Segment 3DPrint software to help the user extract the metal shapes and then run the U-Net network to segmented the region of the scan selected by the user. However, it has been observed that for high attenuating metals such as platinum or gold, a simple thresholding was not sufficient to extract properly the metal shapes because of strong artefacts. It would thus be interesting to see if the artefact-robust DL bone-segmentation tool would provide proper segmentation even with incorrect metal shapes.

Finally, as the initial goal was to use this new segmentation-tool for clinical purposes, it should be documented and tested as required by the FDA and CE-mark requirements. Once this is done, it would then be possible to add it to the current Segment 3DPrint software and make it available for clinical use.



## 6. Conclusion

This study provided a complete pipeline to develop a DL bone-segmentation tool robust to metal artefacts. The metal artefacts simulator has proven to successfully recreate physical phenomena in order to obtain realistic metal artefacts shapes and intensities. Once the metal implants added to the dataset, various synthetic artefacts can be generated automatically. Even if this pipeline was originally oriented towards bone segmentation, it could be easily modified to train other types of DL networks or even provide great augmentation possibilities to standard datasets without metal by rescanning it with the simulator. Noise and other augmentations could be added in a more realistic way and thus provide richer augmentations and potentially more robust networks.





## 7. Appendix

**Table 7.1:** Training data. *Anatomy* refers to anatomical description and details regarding subjective image quality, *Acq. year* refers to year of image acquisition, *Age* refers to age of the patient at image acquisition, *Scanner* is the used scanner, *Res [mm]* is the in plane image resolution in mm, *Mvox* is the number of million voxels in the data set. *U* refers to unknown.

#	Anatomy and pathology	Acq. year	Age (year)	Sex	Scanner	Res [mm]	Mvox
1	Lumbar pelvis, massive calcification in the aorta	U	80	F	Siemens	0.69	148
2	Spine, small amount of contrast agent	U	42	F	Siemens	0.65	71
3	Spine	U	70	M	Siemens	0.72	50
4	Spine	U	60	F	Siemens	0.56	137
5	Skull	U	21	M	Philips	0.43	106
6	Spine	U	52	M	Siemens	0.98	19
7	Feet with metal implant	U	14	F	Siemens	0.26	160
8	Foot	U	61	M	Siemens	0.78	18
9	Foot	U	34	F	Siemens	0.53	39
10	En platta	U	56	U	Toshiba	0.63	33
11	Part of left hand, ulna & radius	U	27	U	Philips	0.45	65
12	Part of right hand, ulna & radius	U	19	U	Philips	0.40	93
13	Left hand	U	70	U	Philips	0.28	132
14	Pelvis	U	2	F	Siemens	0.53	63
15	Pelvis	U	4	M	Philips	0.33	125
16	Spine sever scoliosis (upper part)	U	11	F	Philips	0.49	90
17	Pediatric scoliosis	U	6	M	Siemens	0.53	84
18	Severe scoliosis	U	14	F	Toshiba	0.50	241
19	Standard skull, older subject	U	92	F	Siemens	0.43	91
20	Spine	U	62	F	Philips	0.40	173
21	Spine, heavy lung tumour	1992	34	F	Siemens	0.55	129
22	Spine, contrast agent	1993	76	F	GE	0.53	140
23	Right hand	2021	56	U	Toshiba	0.63	33
24	Part of right hand, ulna & radius	2018	27	U	Philips	0.45	65
25	Left Hand	2019	19	U	Philips	0.40	82
26	Thoracic, Pelvis and part of femur, Marfan syndrome, massive dissected aorta, artificial valve	2020	48	M	Siemens	0.63	295
27	Spine	1990	71	U	GE	0.82	120

#	Anatomy and pathology	Acq. year	Age (year)	Sex	Scanner	Res [mm]	Mvox
28	Both arms (elbow to metacarpals)	U	14	F	Toshiba	0.54	142
29	Part of hands, ulna and radius	U	46	F	Toshiba	0.45	70
30	Thorax, Pelvis and femurs with metal prosthesis on left hip	U		M	GE	1.02	233
31	Left hand	U	62	F	Siemens	0.29	97
32	Right hand	U	62	F	Siemens	0.29	99
33	Arms	U	53	F	Siemens	0.74	111
34	Hip and femurs. Metal hip prosthesis (right hip)	U	27	M	Philips	0.94	162
35	Left foot with artefacts from the L bar	U	69	F	Siemens	0.48	96
36	Mandibula Brackets	U		-	Philips	0.43	32
37	Feet	U	50	M	Siemens	0.54	94
38	Mandibula with metal	U	52	F	Philips	0.39	36
39	Hands and elbows	U	16	F	Siemens	0.30	781
40	Shoulder	U	28	F	Siemens	0.20	222
41	Left hand	U	61	F	Siemens	0.45	107
42	Right hand	U	62	F	Siemens	0.29	135
43	Left hand	U	44	M	Siemens	0.24	357
44	Left thorax	U	23	M	Siemens	0.38	260
45	Right thorax	U	23	M	Siemens	0.38	260
46	Both arms with metal plate on the left arm	U	35	M	Siemens	0.80	125
47	Left foot	U	67	F	Siemens	0.21	227
48	Feet with tibia and fibula	U		F	GE	0.98	32
49	Right thorax	U	58	M	Siemens	0.36	298
50	Upper thorax with metallic wire	U	62	F	Siemens	0.98	53

**Table 7.2:** Test data. *Anatomy* refers to anatomical description and details regarding subjective image quality, *Acq. year* refers to year of image acquisition, *Age* refers to age of the patient at image acquisition, *Scanner* is the used scanner, *Res [mm]* is the in plane image resolution in mm, *Mvox* is the number of million voxels in the data set. *U* refers to unknown.

#	Anatomy and pathology	Acq. year	Age (year)	Sex	Scanner	Res [mm]	Mvox
1	Spine	U	1	F	Philips	0.30	68
2	Hand positioned over the chest. Sever joint disorder	2021	61	F	Siemens	0.52	77
3	Hand data set with ulna and radius	2020	15	F	GE	0.81	61
4	Skull with defect	2018	74	M	Philips	0.43	105
5	Skull with defect	2019	32	F	Siemens	0.43	97
6	Feet	2020	34	F	Siemens	0.48	29
7	Pediatric tumor with contrast on board left	2020	0.4	F	Siemens	0.37	57
8	Semi-thorax (neonate)	2021	0.06	M	Siemens	0.27	26
9	Young pelvis female	2020	2	F	Philips	0.31	105
10	Young pelvis male	2019	1	M	Siemens	0.34	85
11	Knee with contrast on board left	2017	61	M	Siemens	0.79	16
12	Severe scoliosis (lower part)	2019	11	F	Philips	0.49	90
13	Pretty severe scoliosis	2019	14	F	Toshiba	0.50	241
14	Ulna and radius hands and part of spine	U	62	M	Philips	0.49	80
15	Arm right	2021	58	F	Toshiba	0.27	295
16	Mandibula with wires	U	50	M	GE	0.52	21
17	Pelvis with metal plates on the right femur	U	12	M	Philips	0.60	311
18	Pelvis with metal plates on the right femur (DualCT)	U	12	M	Philips	0.60	311
19	Part of right hand with metal plate	U	70	F	Philips	0.29	113
20	Feet	2018	22	F	Siemens	0.61	93
21	Right hand with metal plates	2021	61	F	Siemens	0.23	159
22	Feet	2021	49	M	Siemens	0.53	99
23	Right hand	U	45	M	Philips	0.31	130
24	Brackets top and bottom and many fixations	2022	45	F	Siemens	0.34	65
25	Knees	2022	38	F	Toshiba	0.73	101

**Table 7.3:** Mass attenuation coefficients used for the simulation of metal artefacts. *SS* refers to Stainless steel. Formulas for each material displayed in Table

3.1.

Energy [keV]	Eau [cm <sup>2</sup> /g]	Bone [cm <sup>2</sup> /g]	Titanium [cm <sup>2</sup> /g]	Iron [cm <sup>2</sup> /g]	Nitinol [cm <sup>2</sup> /g]	Gold [cm <sup>2</sup> /g]	Silver [cm <sup>2</sup> /g]	Platinum [cm <sup>2</sup> /g]	SS304 [cm <sup>2</sup> /g]	SS316 [cm <sup>2</sup> /g]	CobaltAlloy [cm <sup>2</sup> /g]	TitaniumAlloy [cm <sup>2</sup> /g]
1	4077	3781	5870	9085	7862	4653	7037	4433	8844	8811	8715	5613
2	617,3	586,9	986	1627	1517	1137	1401	1080	1598	1600	1569	1067
3	192,8	295,8	332	557,6	520,9	2049	513,6	1965	547,5	582,1	656,2	361,3
4	82,77	133,1	152	256,7	240	1144	1305	1100	252	268,9	305,5	165,1
5	42,59	191,7	684	139,9	431,5	666	738,8	640,1	137,3	146,8	167,5	630,8
6	24,64	117,1	432	84,84	270,7	425,2	461,1	408,1	164,4	161,3	237,3	414,8
7	15,5	67,61	283	55,56	177,2	289,1	307,3	277,3	118	114,8	176,1	271,8
8	10,4	37,3	306	305,6	125,9	207,2	216,4	198,7	275,3	268,3	287,5	194
9	7,29	26,8	148	225,7	210,1	153,9	157,9	147,6	221,2	220,8	214,1	141,8
10	5,33	19,9	111	170,7	159,8	118,1	119,3	113,2	168	167,7	163,4	106,1
11	4,03	15,2	85	132,3	124,1	92,83	92,13	88,99	130,5	130,3	127,3	81,46
12	3,13	11,9	66,8	104,7	98,23	183,7	72,84	176,4	103,3	103,1	100,8	64,01
13	2,49	9,48	53,5	84,33	79,01	148,4	58,71	142,6	83,11	82,98	81,07	51,26
14	2,02	7,69	43,5	68,94	64,49	168,5	48,1	187,9	67,86	67,77	66,15	41,69
15	1,67	6,33	35,9	57,09	53,34	163,7	39,98	157,8	56,14	56,07	54,7	34,36
16	1,41	5,27	29,9	47,79	44,64	138,9	33,55	133,8	46,98	46,93	45,77	28,64
17	1,2	4,45	25,2	40,41	37,75	119,1	28,46	114,6	39,72	39,68	38,71	24,12
18	1,04	3,79	21,4	34,47	32,22	103	24,39	99,05	33,88	33,85	33,04	20,5
19	0,913	3,26	18,4	29,65	27,72	89,76	21,08	86,3	29,14	29,12	28,43	17,58
20	0,81	2,83	15,9	25,68	24,03	78,81	18,36	75,73	25,25	26,56	29,3	15,18
21	0,725	2,48	13,8	22,4	20,96	69,4	16,08	66,68	22,02	23,33	26,14	13,2
22	0,656	2,18	12,1	19,65	18,39	61,48	14,18	59,06	19,32	20,56	23,26	11,56
23	0,598	1,94	10,6	17,34	16,23	54,77	12,58	52,6	17,05	18,18	20,67	10,18
24	0,549	1,73	9,41	15,38	14,4	49,03	11,22	47,09	15,12	16,14	18,36	9,011
25	0,508	1,56	8,37	13,7	12,83	44,1	10,06	42,35	13,47	14,37	16,33	8,018
26	0,473	1,4	7,48	12,26	11,48	39,84	9,21	38,25	12,05	12,84	14,55	7,167
27	0,443	1,28	6,72	11,02	10,32	36,13	8,48	34,69	10,83	11,52	13,01	6,434
28	0,418	1,16	6,05	9,942	9,309	32,89	7,76	31,57	9,722	10,38	11,68	5,8
29	0,395	1,07	5,48	9,001	8,429	30,04	7,16	28,83	8,847	9,381	10,53	5,247
30	0,376	0,982	4,97	8,176	7,657	27,52	6,668	26,41	8,036	8,513	9,531	4,764
31	0,358	0,908	4,53	7,451	6,979	25,25	6,237	24,23	7,323	7,753	8,669	4,364
32	0,343	0,842	4,14	6,81	6,38	23,23	5,83	22,3	6,693	7,085	7,919	3,97
33	0,33	0,785	3,79	6,242	5,848	21,44	5,48	20,57	6,135	6,494	7,29	3,636
34	0,318	0,733	3,49	5,737	5,376	19,83	5,16	19,02	5,638	5,97	6,678	3,342
35	0,308	0,688	3,21	5,285	4,954	18,38	4,84	17,63	5,195	5,503	6,161	3,08
36	0,298	0,647	2,97	4,881	4,576	17,08	4,56	16,38	4,798	5,085	5,699	2,846
37	0,289	0,61	2,75	4,518	4,237	15,9	4,31	15,25	4,441	4,71	5,285	2,637
38	0,282	0,577	2,55	4,192	3,932	14,83	4,07	14,23	4,12	4,371	4,911	2,448
39	0,275	0,548	2,37	3,896	3,656	13,86	3,84	13,29	3,83	4,066	4,572	2,278
40	0,268	0,521	2,21	3,629	3,406	12,98	3,63	12,45	3,568	3,789	4,265	2,124
41	0,263	0,496	2,07	3,387	3,18	12,17	3,43	11,67	3,33	3,537	3,984	1,985
42	0,257	0,474	1,94	3,166	2,974	11,43	3,24	10,95	3,113	3,308	3,728	1,859
43	0,252	0,454	1,82	2,965	2,786	10,74	3,07	10,3	2,916	3,098	3,493	1,744
44	0,248	0,436	1,71	2,782	2,615	10,12	2,92	9,698	2,735	2,907	3,278	1,639
45	0,244	0,419	1,61	2,614	2,458	9,542	2,78	9,146	2,57	2,732	3,081	1,543
46	0,24	0,403	1,51	2,46	2,314	9,011	2,65	8,636	2,419	2,571	2,899	1,455
47	0,236	0,389	1,43	2,318	2,182	8,521	2,53	8,166	2,28	2,423	2,733	1,374
48	0,233	0,376	1,35	2,188	2,06	8,068	2,42	7,731	2,152	2,287	2,579	1,3
49	0,23	0,364	1,28	2,068	1,948	7,648	2,32	7,328	2,034	2,161	2,437	1,231
50	0,227	0,352	1,21	1,957	1,844	7,258	2,23	6,954	1,926	2,046	2,306	1,168
51	0,224	0,342	1,15	1,855	1,748	6,893	2,14	6,604	1,825	1,939	2,185	1,11
52	0,222	0,332	1,1	1,76	1,659	6,553	2,06	6,279	1,732	1,839	2,073	1,056
53	0,219	0,323	1,04	1,672	1,577	6,237	1,98	5,976	1,645	1,747	1,969	1,006
54	0,217	0,315	0,995	1,591	1,5	5,942	1,91	5,694	1,565	1,662	1,872	0,9591
55	0,215	0,307	0,95	1,515	1,429	5,667	1,84	5,429	1,49	1,583	1,782	0,9159
56	0,213	0,3	0,908	1,444	1,363	5,409	1,77	5,182	1,421	1,509	1,698	0,8756
57	0,211	0,293	0,869	1,378	1,301	5,167	1,71	4,951	1,356	1,439	1,62	0,8381
58	0,209	0,287	0,832	1,316	1,243	4,941	1,65	4,734	1,296	1,375	1,547	0,8031
59	0,208	0,281	0,798	1,259	1,189	4,729	1,6	4,531	1,239	1,315	1,479	0,7704
60	0,206	0,275	0,766	1,205	1,139	4,529	1,55	4,34	1,186	1,258	1,415	0,7399
61	0,204	0,27	0,736	1,154	1,091	4,34	1,5	4,159	1,136	1,206	1,355	0,7112
62	0,203	0,265	0,708	1,107	1,047	4,162	1,45	3,988	1,09	1,156	1,298	0,6844
63	0,201	0,26	0,682	1,063	1,005	3,995	1,4	3,828	1,046	1,109	1,245	0,6592
64	0,2	0,256	0,657	1,021	0,9663	3,837	1,36	3,677	1,005	1,066	1,196	0,6355
65	0,199	0,252	0,634	0,9816	0,9295	3,688	1,31	3,534	0,9666	1,024	1,149	0,6132
66	0,197	0,248	0,612	0,9446	0,8949	3,547	1,27	3,399	0,9303	0,9857	1,105	0,5923
67	0,196	0,244	0,591	0,9097	0,8623	3,414	1,23	3,271	0,896	0,9491	1,063	0,5725
68	0,195	0,24	0,572	0,8768	0,8315	3,287	1,19	3,15	0,8637	0,9146	1,024	0,5539
69	0,194	0,237	0,554	0,8457	0,8024	3,168	1,15	3,036	0,8332	0,8821	0,987	0,5363
70	0,193	0,234	0,536	0,8164	0,775	3,054	1,11	2,927	0,8044	0,8513	0,952	0,5197

...	...	...	...	...	...	...	...	...	...	...	...	...
71	0,192	0,231	0,52	0,7886	0,749	2,947	3,66	2,824	0,7771	0,8222	0,9189	0,504
72	0,191	0,228	0,504	0,7623	0,7244	2,844	3,52	2,726	0,7513	0,7946	0,8876	0,4891
73	0,19	0,225	0,489	0,7374	0,7011	2,747	3,39	2,633	0,7269	0,7685	0,8578	0,475
74	0,189	0,222	0,476	0,7138	0,679	2,655	3,27	2,545	0,7037	0,7438	0,8297	0,4616
75	0,188	0,22	0,462	0,6915	0,6581	2,567	3,15	2,461	0,6817	0,7203	0,8029	0,4489
76	0,187	0,217	0,45	0,6702	0,6382	2,483	3,04	2,381	0,6608	0,698	0,7776	0,4369
77	0,186	0,215	0,438	0,65	0,6193	2,403	2,94	2,304	0,641	0,6768	0,7534	0,4254
78	0,185	0,213	0,426	0,6308	0,6013	2,327	2,84	2,231	0,6222	0,6567	0,7305	0,4145
79	0,185	0,211	0,416	0,6126	0,5842	2,255	2,74	9,126	0,6042	0,6376	0,7087	0,4042
80	0,184	0,209	0,405	0,5952	0,5679	2,185	2,65	8,732	0,5872	0,6193	0,6879	0,3943
81	0,183	0,207	0,395	0,5787	0,5524	8,825	2,56	8,376	0,5709	0,6019	0,6681	0,3849
82	0,182	0,205	0,386	0,5629	0,5376	8,552	2,48	8,054	0,5554	0,5854	0,6492	0,3759
83	0,181	0,203	0,377	0,5478	0,5235	8,292	2,4	7,763	0,5406	0,5696	0,6312	0,3674
84	0,181	0,201	0,369	0,5335	0,51	8,042	2,33	7,497	0,5265	0,5545	0,614	0,3592
85	0,18	0,2	0,361	0,5198	0,4971	7,802	2,25	7,254	0,5131	0,5401	0,5976	0,3514
86	0,179	0,198	0,353	0,5067	0,4848	7,573	2,19	7,031	0,5002	0,5264	0,5819	0,3439
87	0,179	0,196	0,345	0,4942	0,4731	7,353	2,12	6,825	0,4879	0,5132	0,5669	0,3368
88	0,178	0,195	0,338	0,4822	0,4618	7,141	2,06	6,634	0,4761	0,5006	0,5526	0,3299
89	0,177	0,194	0,331	0,4707	0,4511	6,938	2	6,456	0,4649	0,4886	0,5388	0,3234
90	0,177	0,192	0,325	0,4597	0,4407	6,744	1,94	6,289	0,4541	0,4771	0,5257	0,3171
91	0,176	0,191	0,318	0,4492	0,4309	6,556	1,88	6,132	0,4438	0,466	0,5131	0,3111
92	0,175	0,189	0,312	0,4391	0,4214	6,377	1,83	5,984	0,4338	0,4554	0,501	0,3053
93	0,175	0,188	0,307	0,4295	0,4123	6,203	1,78	5,843	0,4243	0,4453	0,4894	0,2998
94	0,174	0,187	0,301	0,4202	0,4036	6,037	1,73	5,709	0,4152	0,4355	0,4783	0,2945
95	0,174	0,186	0,296	0,4113	0,3952	5,877	1,68	5,58	0,4065	0,4262	0,4676	0,2894
96	0,173	0,185	0,291	0,4028	0,3872	5,722	1,64	5,455	0,3981	0,4172	0,4574	0,2844
97	0,172	0,183	0,286	0,3945	0,3795	5,573	1,59	5,335	0,39	0,4086	0,4475	0,2797
98	0,172	0,182	0,281	0,3866	0,372	5,43	1,55	5,218	0,3822	0,4003	0,4381	0,2752
99	0,171	0,181	0,277	0,3791	0,3649	5,292	1,51	5,105	0,3748	0,3923	0,429	0,2708
100	0,171	0,18	0,272	0,3717	0,358	5,158	1,47	4,993	0,3676	0,3846	0,4202	0,2666
101	0,17	0,179	0,268	0,3647	0,3514	5,03	1,43	4,884	0,3607	0,3772	0,4118	0,2626
102	0,17	0,178	0,264	0,3579	0,345	4,906	1,4	4,777	0,354	0,3701	0,4036	0,2586
103	0,169	0,177	0,26	0,3514	0,3389	4,786	1,36	4,672	0,3476	0,3633	0,3958	0,2549
104	0,169	0,176	0,256	0,3451	0,333	4,67	1,33	4,569	0,3414	0,3567	0,3883	0,2512
105	0,168	0,176	0,252	0,3391	0,3273	4,558	1,3	4,469	0,3355	0,3503	0,381	0,2477
106	0,168	0,175	0,249	0,3332	0,3218	4,45	1,26	4,37	0,3297	0,3441	0,374	0,2444
107	0,167	0,174	0,246	0,3276	0,3165	4,345	1,23	4,274	0,3242	0,3382	0,3672	0,2411
108	0,167	0,173	0,242	0,3221	0,3113	4,244	1,21	4,18	0,3188	0,3325	0,3607	0,2379
109	0,166	0,172	0,239	0,3169	0,3064	4,146	1,18	4,088	0,3137	0,327	0,3544	0,2349
110	0,166	0,171	0,236	0,3118	0,3016	4,051	1,15	3,998	0,3087	0,3216	0,3483	0,2319
111	0,165	0,171	0,233	0,3069	0,297	3,96	1,12	3,911	0,3038	0,3165	0,3424	0,2291
112	0,165	0,17	0,23	0,3021	0,2925	3,871	1,1	3,825	0,2992	0,3115	0,3367	0,2263
113	0,164	0,169	0,227	0,2975	0,2882	3,785	1,07	3,742	0,2947	0,3067	0,3312	0,2236
114	0,164	0,168	0,225	0,2931	0,284	3,702	1,05	3,66	0,2903	0,302	0,3259	0,221
115	0,164	0,168	0,222	0,2888	0,28	3,621	1,03	3,581	0,2861	0,2975	0,3208	0,2185
116	0,163	0,167	0,22	0,2846	0,2761	3,543	1,01	3,503	0,282	0,2931	0,3158	0,2161
117	0,163	0,166	0,217	0,2806	0,2723	3,467	0,98	3,428	0,278	0,2889	0,311	0,2137
118	0,162	0,166	0,215	0,2767	0,2686	3,393	0,96	3,354	0,2742	0,2848	0,3063	0,2115
119	0,162	0,165	0,212	0,2729	0,2651	3,322	0,94	3,283	0,2705	0,2808	0,3018	0,2092
120	0,1614	0,164	0,2102	0,2693	0,2616	3,252	0,924	3,213	0,2669	0,277	0,2974	0,2071
121	0,1609	0,163	0,208	0,2657	0,2583	3,185	0,9051	3,145	0,2634	0,2733	0,2931	0,205
122	0,1605	0,163	0,2059	0,2623	0,255	3,12	0,8869	3,079	0,26	0,2696	0,289	0,203
123	0,1601	0,162	0,2038	0,2589	0,2519	3,056	0,8692	3,014	0,2567	0,2661	0,285	0,201
124	0,1597	0,162	0,2019	0,2557	0,2488	2,994	0,8521	2,951	0,2535	0,2627	0,2812	0,1991
125	0,1593	0,1614	0,1999	0,2526	0,2459	2,935	0,8354	2,89	0,2504	0,2594	0,2774	0,1972
126	0,1589	0,1609	0,198	0,2495	0,243	2,876	0,8193	2,831	0,2474	0,2562	0,2737	0,1954
127	0,1586	0,1605	0,1962	0,2465	0,2402	2,82	0,8036	2,773	0,2445	0,2531	0,2702	0,1937
128	0,1582	0,1601	0,1944	0,2437	0,2375	2,765	0,7884	2,716	0,2417	0,2501	0,2667	0,1919
129	0,1578	0,1597	0,1927	0,2409	0,2348	2,711	0,7737	2,661	0,2389	0,2471	0,2634	0,1903
130	0,1574	0,1593	0,191	0,2381	0,2323	2,659	0,7593	2,608	0,2362	0,2443	0,2601	0,1886
131	0,157	0,1589	0,1894	0,2355	0,2298	2,608	0,7454	2,556	0,2336	0,2415	0,257	0,1871
132	0,1567	0,1586	0,1878	0,2329	0,2273	2,559	0,7319	2,505	0,2311	0,2388	0,2539	0,1855
133	0,1563	0,1582	0,1862	0,2304	0,225	2,511	0,7188	2,456	0,2286	0,2362	0,2509	0,184
134	0,1559	0,1578	0,1847	0,228	0,2227	2,464	0,706	2,408	0,2262	0,2336	0,248	0,1826
135	0,1556	0,1574	0,1832	0,2256	0,2204	2,419	0,6936	2,362	0,2239	0,2311	0,2452	0,1811
136	0,1552	0,157	0,1818	0,2233	0,2182	2,375	0,6815	2,316	0,2216	0,2287	0,2424	0,1797
137	0,1549	0,1567	0,1804	0,221	0,2161	2,331	0,6698	2,272	0,2194	0,2263	0,2397	0,1784
138	0,1545	0,1563	0,179	0,2188	0,214	2,289	0,6584	2,229	0,2173	0,224	0,2371	0,1771
139	0,1542	0,1559	0,1777	0,2167	0,212	2,248	0,6472	2,187	0,2152	0,2218	0,2346	0,1758
140	0,1538	0,1556	0,1764	0,2146	0,2101	2,209	0,6364	2,147	0,2131	0,2196	0,2321	0,1745

# References

- [1] B. DE MAN, J. NUYTS, P. DUPONT, G. MARCHAL, AND P. SUETENS. **Metal streak artifacts in X-ray computed tomography: a simulation study.** *IEEE Transactions on Nuclear Science*, **46**(3):691–696, 1999. [9](#)
- [2] DROSOULA GIANTSOU, BRUNO DE MAN, JOOST VERBURG, ALEXEI TROFIMOV, YANNAN JIN, GE WANG, LARS GJESTEBY, AND HARALD PAGANETTI. **Metal artifacts in computed tomography for radiation therapy planning: dosimetric effects and impact of metal artifact reduction.** *Physics in Medicine & Biology*, **62**(8):R49, mar 2017. [9](#)
- [3] MOHAMMAD HESAM HESAMIAN, WENJING JIA, XIANGJIAN HE, AND PAUL KENNEDY. **Deep Learning Techniques for Medical Image Segmentation: Achievements and Challenges.** *Journal of Digital Imaging*, **32**, 05 2019. [9](#) [10](#) [11](#)
- [4] MITSUKI SAKAMOTO, YUTA HIASA, YOSHITO OTAKE, MASAKI TAKAO, YUKI SUZUKI, NOBUHIKO SUGANO, AND YOSHINOBU SATO. **Automated Segmentation of Hip and Thigh Muscles in Metal Artifact-Contaminated CT using Convolutional Neural Network-Enhanced Normalized Metal Artifact Reduction.** *In International Forum on Medical Imaging in Asia 2019*, 06 2019. [10](#) [19](#) [25](#) [27](#)
- [5] OLAF RONNEBERGER, PHILIPP FISCHER, AND THOMAS BROX. **U-Net: Convolutional Networks for Biomedical Image Segmentation.** *LNCS*, **9351**:234–241, 10 2015. [10](#)
- [6] H. ERDOGAN AND J.A. FESSLER. **Monotonic algorithms for transmission tomography.** *IEEE Transactions on Medical Imaging*, **18**(9):801–814, 1999. [13](#)
- [7] DONALD L. SNYDER, CARL W. HELSTROM, AARON D. LANTERMAN, MOHAMMAD FAISAL, AND RICHARD L. WHITE. **Compensation for readout noise in CCD images.** *J. Opt. Soc. Am. A*, **12**(2):272–283, Feb 1995. [13](#)
- [8] IDRIS ELBAKRI AND JEFFREY FESSLER. **Statistical Image Reconstruction for Polyenergetic X-Ray Computed Tomography.** *IEEE transactions on medical imaging*, **21**:89–99, 03 2002. [13](#) [28](#)
- [9] QIONG XU, HENGYONG YU, XUANQIN MOU, LEI ZHANG, JIANG HSIEH, AND GE WANG. **Low-Dose X-ray CT Reconstruction via Dictionary Learning.** *IEEE transactions on medical imaging*, **31**:1682–97, 04 2012. [13](#)
- [10] R. SCHOFIELD, L. KING, U. TAYAL, I. CASTELLANO, J. STIRRUP, F. PONTANA, J. EARLS, AND E. NICOL. **Image reconstruction: Part 1 – understanding filtered back projection, noise and image acquisition.** *Journal of Cardiovascular Computed Tomography*, **14**(3):219–225, 2020. [14](#)
- [11] FRANZ BOAS AND DOMINIK FLEISCHMANN. **CT artifacts: Causes and reduction techniques.** *Imaging in Medicine*, **4**, 04 2012. [15](#)
- [12] ANAND VELLARACKAL AND ACHIM KAIM. **Metal artefact reduction of different alloys with dual energy computed tomography (DECT).** *Scientific Reports*, **11**:2211, 01 2021. [15](#)

- [13] TYLER COUPAL, PAUL MALLINSON, PATRICK MC LAUGHLIN, SAVVAS NICOLAOU, PETER MUNK, AND HUGUE OUELLETTE. **Peering through the glare: Using dual-energy CT to overcome the problem of metal artefacts in bone radiology.** *Skeletal radiology*, **43**, 01 2014. [16](#)
- [14] R.H.H. WELLENBERG, E.T. HAKVOORT, C.H. SLUMP, M.F. BOOMSMA, M. MAAS, AND G.J. STREEKSTRA. **Metal artifact reduction techniques in musculoskeletal CT-imaging.** *European Journal of Radiology*, **107**:60–69, 2018. [16](#)
- [15] YANBO ZHANG AND HENGYONG YU. **Convolutional Neural Network Based Metal Artifact Reduction in X-Ray Computed Tomography.** *IEEE Transactions on Medical Imaging*, **37**(6):1370–1381, 2018. [17](#) [26](#) [27](#)
- [16] YANBO ZHANG, XUANQIN MOU, AND SHAOJIE TANG. **Beam hardening correction for fan-beam CT imaging with multiple materials.** *Nuclear Science Symposium Conference Record (NSS/MIC)*, 2010 *IEEE*, 10 2010. [17](#)
- [17] HYOUNG PARK, DOSIK HWANG, AND JIN SEO. **Metal Artifact Reduction for Polychromatic X-ray CT Based on a Beam-Hardening Corrector.** *IEEE transactions on medical imaging*, **35**, 09 2015. [17](#)
- [18] MARC KACHELRIESS, OLIVER WATZKE, AND WILLI KALENDER. **Generalized multi-dimensional adaptive filtering for conventional and spiral single-slice, multi-slice, and cone-beam CT.** *Medical physics*, **28**:475–90, 05 2001. [17](#)
- [19] THE MATHWORKS INC. **MATLAB version: 9.13.0 (R2022b)**, 2022. [19](#)
- [20] LONG BAI, CHENG GONG, XIAOHONG CHEN, YUANXI SUN, JUNFANG ZHANG, LECAI CAI, SHENGYAN ZHU, AND SHENG QUAN XIE. **Additive Manufacturing of Customized Metallic Orthopedic Implants: Materials, Structures, and Surface Modifications.** *Metals*, **9**(9), 2019. [21](#) [24](#)
- [21] JOSÉ VANZIN, DANIEL ABUD, MARCO TULLIO REZENDE, AND JACQUES MORET. **Number of coils necessary to treat cerebral aneurysms according to each size group: A study based on a series of 952 embolized aneurysms.** *Arquivos de neuro-psiquiatria*, **70**:520–3, 07 2012. [22](#)
- [22] MDNALI. **126 Typical Densities Of Metals And Alloys**, 4 2021. [24](#) [26](#)
- [23] GARY H. GLOVER. **Compton scatter effects in CT reconstructions.** *Medical Physics*, **9**:860–867, 1982. [26](#)
- [24] P M JOSEPH AND R D SPITAL. **The effects of scatter in x-ray computed tomography.** *Med. Phys.; (United States)*, **9**:4, 1982. [26](#)
- [25] SIEMENS HEALTHINEERS. **Simulation of x-ray spectra.** [27](#) [28](#) [29](#)
- [26] M.J. BERGER, J.H. HUBBELL, S.M. SELTZER, J. CHANG, J.S. COURSEY, D.S. SUKUMAR, R. AND ZUCKER, AND K OLSEN. **XCOM: Photon Cross Section Database.** *National Institute of Standards and Technology, Gaithersburg, MD.*, 2010. [29](#)
- [27] **Tissue substitutes in radiation dosimetry and measurement** 1 1989. [29](#)
- [28] G T HERMAN. **Correction for beam hardening in computed tomography.** *Physics in Medicine & Biology*, **24**(1):81, jan 1979. [29](#)
- [29] MOHAMMAD NASER, ADNAN MAHMUD, TANZIL MAHMUD AREFIN, GOLAM SAROWAR, AND M M NAUSHAD ALI. **Comparative analysis of Radon and Fan-beam based feature extraction techniques for Bangla character recognition.** 01 2009. [30](#) [31](#)
- [30] A. AVERBUCH, ILYA SEDELNIKOV, AND YOEL SHKOLNISKY. **CT Reconstruction From Parallel and Fan-Beam Projections by a 2-D Discrete Radon Transform.** *Image Processing, IEEE Transactions on*, **21**:733 – 741, 03 2012. [31](#)



- [31] AMADEUS ALCANTARA, ISRAEL ASSIS, DANIEL PRADA, KONRAD MEHLE, STEFAN SCHWAN, LUCIA COSTA-PAIVA, MUNIR SKAF, LUIZ WROBEL, AND PAULO SOLLERO. **Patient-Specific Bone Multiscale Modelling, Fracture Simulation and Risk Analysis—A Survey.** *Materials*, **13**:106, 12 2019. [31](#)
- [32] C GLIDE-HURST, DANWEN CHEN, HUALIANG ZHONG, AND INDRIN CHETTY. **Changes realized from extended bit-depth and metal artifact reduction in CT.** *Medical physics*, **40**, 06 2013. [31](#)
- [33] BENNSTRÖM, ANDREAS AND WINZELL, FILIP. **Automated 3D Bone Segmentation using Deep Learning in Scoliosis**, 2021. Student Paper. [33](#)
- [34] CONNOR SHORTEN AND TAGHI M. KHOSHGOFTAAR. **A survey on Image Data Augmentation for Deep Learning.** *Journal of Big Data*, **6**:1–48, 2019. [35](#)
- [35] AMIR AVERBUCH AND YOEL SHKOLNISKY. **3D Fourier based discrete Radon transform** *Applied and Computational Harmonic Analysis*, **15**(1):33–69, 2003. [49](#)